INFLUENCE OF MOLECULAR WEIGHT, TEMPERATURE AND EXTENSIONAL RHEOLOGY ON MELT BLOWING PROCESS STABILITY FOR LINEAR ISOTACTIC POLYPROPYLENE

Jiri Drabek and Martin Zatloukal*

Polymer Centre, Faculty of Technology, Tomas Bata University in Zlín,

Vavrečkova 275, 760 01 Zlín, Czech Republic

Keywords: Polymer melt, extensional rheology, viscoelasticity, linear isotactic polypropylene, meltblown, flow stability.

*Corresponding author: mzatloukal@utb.cz

ABSTRACT

In this work, three linear isotactic polypropylenes with different weight-average molecular weights, M_w, and comparable polydispersity were used to produce nonwovens by melt blowing technology at two different temperatures, T. The air/polymer flow rate was changed to maintain the same average fiber diameter, resulting in a different broadness of fiber diameter distribution, which was quantified by the coefficient of variation, CV. The elasticity of the material was evaluated by the Reptation-mode relaxation time, λ_1, and the Rouse-mode reorientation time, λ_2, determined from the deformation rate dependent shear viscosity data. Extensional rheology was evaluated using uniaxial extensional viscosity measured over a very wide range of strain rates (2×10^4 – 2×10^6 1/s) using entrance pressure drop and Gibson method. Obtained plateau value of uniaxial extensional viscosity at the highest extensional strain rates, $\eta_{E,\infty}$, (normalized by the three times zero-shear rate viscosity, η_0) and the minimum uniaxial extensional viscosity, $\eta_{E,min}$ were related to M_w and T using simple equations. It has been found that the stability of fibers production captured by CV depends exclusively on the extensional properties of the polypropylene melts, namely $\frac{\eta_{E,U,\infty}}{3\eta_0}$ and $\eta_{E,U,min}$. These findings are important especially with regard to the stable production of polymeric nanofibers by melt blowing technology.

INTRODUCTION

Meltblown (MB) is a one-step process for converting polymeric raw materials into nonwovens with many applications, such as filtration (air or liquid) surgical face masks and gowns, protective overalls, drapes, battery separators, sorbents and wipes, hygiene (diapers, nappies, towels), biosensors, scaffolds for tissue engineering and many other areas [1 – 3]. In this technology, the polymer melt is extruded through small holes into converging hot air streams [4 – 6], typically reaching 50 – 80 % of the speed of sound [2, 7, 8]. The drag force of the air causes a rapid elongation of the melt into a fine fiber with a small diameter [4 – 6], as shown in Figure 1. A typical change in fiber diameter (expressed here as the ratio of die to final fiber diameter), is between 250 and 667 for isotactic polypropylenes [9, 10]. It has been reported that the highest reduction in fiber diameter occurs at very small post die distances (usually between 10 and 20 mm) and at very short times (0.05 ms) [11 – 14]. During fiber thinning process, very high extensional strain rates ($\sim 10^6$ 1/s) are achieved [15]. The collector captures attenuated filament streams, resulting in a nonwoven web formation with an almost random network of fibers [2]. The typical fiber diameter range for MB is 1 – 2 μm [2, 10, 16, 17], but in many studies published in recent decades, the average fiber diameter is less than 1 μm [1, 4, 10, 16, 18 – 22] and the lowest average fiber diameter ever produced by MB is 36 nm [21].) Polypropylene (PP) is one of the most popular polymers in MB due to its ease of processing and suitability for end use. However, there are flow phenomena (such as whipping [23], fiber breakup, flies, generation of small isolated spherical particles, jam, die drool [24 – 30] and interconnected extrudate swell [31 – 36], secondary flow [37 – 39] and shots), which significantly increases the unevenness of the polymeric fibers produced [40]. It has been shown that the coefficient of variation, *CV*, for the average fiber diameter, d_{av}, can be reduced for polystyrene [15] and PP [9] by increasing the longest melt relaxation time, λ_1,

or introducing a chain branching (maintaining the same molecular weight and polydispersity of PP), which was attributed to the change in the extensional viscosity. In more detail, the stabilizing effect of chain branching has been attributed to facilitating the intensive fiber thinning process due to reduced extensional viscosity at very high strain rates on the one hand and reduced melt sensitivity to whipping instability due to increased extensional viscosity at medium and low strain rates on the other. Larson and Desai [41] showed for the linear polystyrene, based on the finitely extensible nonlinear elastic model (FENE-P) Doi-Edwards-Marrucci-Grizzuti (DEMG) constitutive equations and supporting data, that as the concentration increases from unentangled dilute, to entangled, to a dense melt, the extensional strain hardening at very high extensional strain rates decreases due to the orientation-induced reduction in friction. This suggests that the molecular characteristics and temperature of linear PPs can affect alignment of polymer chains, monomeric friction and high extensional rate rheology, which is key to understanding the stability of the melt blowing process.

To understand molecular structure–rheology–process temperature–flow stability relations for polymer melts at very high strain rates, three well-characterized linear isotactic polypropylenes (molar mass from 56 to 76 kg/mol) were used to produce nonwovens of comparable average fiber diameter on a multihole Reifenhäuser Reicofil pilot plant meltblown line at two different temperatures. The flow stability was quantified in terms of the coefficient of variation, *CV*, charactering the broadness of the fiber diameter distribution.

EXPERIMENTAL

Materials

Linear isotactic polypropylenes (L-PP) Borflow HL504FB, HL508FB and HL512FB produced by Borealis Polyolefine (Linz, Austria), were used in this work. All three samples were carefully characterized in our previous work at 190, 210 and 230 °C by rotational and capillary rheometry as well as by an instrumented injection molding machine to cover a very wide range of shear rates [42] (see Figure 2 – left). The performed measurements allowed direct determination of the zero-shear rate viscosity, η_0, and the infinite shear viscosity, η_∞, together with the corresponding flow activation energies (E_0 and E_∞) using a well-known Arrhenius plot. All the above parameters of the polymers used together with the basic molecular characteristics are given in Table 1. The power-law index, n, the reptation-mode relaxation time, λ_1, and the Rouse-mode reorientation time, λ_2, characterizing the melt elasticity at low and very high shear rates, respectively, represent additional key rheological parameters. However, their determination by fitting of shear viscosity data over a very wide range of shear rates by conventional viscosity models can lead to non-physical values despite giving an excellent numerical fit [9]. In this work, n, λ_1 and λ_2 were determined directly from the measured shear viscosity data as follows. First, tangents were constructed in the area of the first and second Newtonian plateaus. Second, three points were selected just before the beginning of the second Newtonian plateau. Third, the points were fitted by a straight line and the correlation coefficient was calculated. Fourth, additional points were added to these base points step by step (towards lower shear rate values) and the corresponding correlation coefficient was calculated for each individual linear fit. Fifth, the power-law region was determined by the number of points, which led to the highest linear correlation coefficient. Note that for all three samples, the optimal number of points was 16 (see Figure 2 – right). Finally,

the parameters λ_1 and λ_2 were determined as the reciprocal values of the shear rates determined from the intersections between the power-law tangent and the first and second Newtonian plateau tangents (see Figure 2 – left). The parameter *n* is given by the power-law tangent slope, which is equal to n-1. The obtained parameters (i.e. λ_1, λ_2 and *n*) are given in Table 2.

The extensional viscosities for all investigated samples were determined from the measured entrance pressure drop data on the instrumented injection molding machine [42, 43] using the Gibson model, which is based on the sink flow kinematics with no vortices and it is given by the following equations [44 – 46]:

$$\sigma_E = \frac{\overline{P_{Ent}}}{\left[2/(3k)\right]\left[1-(R/R_b)^{3k}\right] + \left\{I(k,\alpha)/\left[\sin(\alpha)(1+\cos(\alpha))\right]^n\right\}} \tag{1}$$

$$\overline{P_{Ent}} = P_{Ent} - 2\tau_{xy,Cor}\left[\sin(\alpha)\right]^{3n}\left[1-(R/R_b)^{3n}\right]\left[(3n+1)/(4n)\right]^n / \left[3n(\pi/2)^{3n+1}\right] \tag{2}$$

$$I(k,\alpha) = \int_0^{\alpha}\left[1+\cos(\beta)\right]^{k-1}\left[\sin(\beta)\right]^{k+1}d\beta \tag{3}$$

$$\dot{\varepsilon} = \frac{1}{4}\dot{\gamma}_{App}\sin(\alpha)\left[1+\cos(\alpha)\right] \tag{4}$$

Here $\overline{P_{Ent}}$ represents the entrance pressure drop arising only from the uniaxial extensional flow, *R* is the radius of the die, R_b is the radius of the barrel, α is the entrance angle, *n* is the local slope in the corrected shear stress ($\tau_{xy,Cor}$) vs. the apparent shear rate ($\dot{\gamma}_{App}$) function in the log-log scale, *k* represents the local slope in the $\overline{P_{Ent}}$ vs. $\dot{\gamma}_{App}$ function in the log-log scale. The term $I(k,\alpha)$ given by Eq. 3 must be calculated numerically.

Melt blowing experiment

L-PP nonwovens were made on the Reifenhäuser Reicofil pilot plant meltblown line (see Figure 3 and the corresponding video below) utilizing a nosepiece die (having sharp-edged die-nose) with the following characteristics: total and active width equal to 350 mm and 250 mm, respectively; orifice diameter: 0.4 mm; number of holes per active part: 470; processing conditions: melt/air temperature: 250 and 270 °C; collector belt speed: 5 m/min, die-to-collector distances: 500 mm. The air volume flow rate was reduced with reduced temperature or increased molecular weight of the polypropylenes used to achieve a comparable average fiber diameter for all samples, i.e. about 1.5 μm, while the mass flow rate for one orifice remained the same (0.0885 g/hole/min). Information on the air volume flow rate used in each case is given in Table 3.

Morphological characterization

For the given processing conditions and the polymer used, two samples with dimensions 10 mm × 10 mm were cut out from different places of the produced nonwoven sample. A HITACHI Tabletop TM-1000 scanning electron microscope (SEM) was then used to visualize the nonwoven structure for each sample at three different magnifications (500×, 1000×, 2500×) by using a high-sensitive back-scattered electron (BSE) detector. The basic morphological characteristics of the produced nonwovens were determined by using in-house developed software (UTBsoft Filtration) at the Faculty of Technology, Tomas Bata University in Zlín. This software makes it possible to combine all three SEM images with different magnifications and to create one normalized fiber diameter distribution curve via skeletonization image processing according to the technique proposed in [9, 47, 48]. This allows to take into account both nanofibers and microfibers, which

appear in manufactured meltblown nonwovens [9]. Mean, d_{av}, standard deviation, σ, and coefficient of variation, *CV* were determined by fitting the fiber diameter distribution by a log-normal function utilizing the following equations [10, 15, 21, 49]:

$$f\left(log\left(d\right)\right)=\frac{1}{\sigma\sqrt{2\pi}}\exp\left[-\frac{1}{2\sigma^2}\left\{\log\left(d\right)-\mu\right\}^2\right] \tag{5}$$

$$d_{av}=10^{\mu\pm\sigma} \tag{6}$$

$$CV=\sqrt{exp\left(\sigma^2\right)-1} \tag{7}$$

RESULTS AND DISCUSSION

Shear rheology

The reptation-mode relaxation time, λ_1, and the Rouse-mode reorientation time, λ_2, were plotted in Figure 4 as a function of the weight-average molecular weight, M_w, at 230 °C. As can be seen, both parameters are linearly scaled with M_w in log-log scale and the power-law exponent for λ_1 is higher (3.139) compared to λ_2 (1.351) and its values are similar to the values obtained for zero shear, η_0, (3.62 [9, 43]) and infinite, η_∞, (1 [9, 43]) viscosities. Since λ_1 and λ_2 relate to highly entangled and almost disentangled states, their temperature dependences can be considered the same as for their shear viscosity counterparts η_0 and η_∞, i.e.

$$\lambda_1=5.807\cdot10^{-19}\exp\left[\frac{E_0}{R}\left(\frac{1}{T}-\frac{1}{T_r}\right)\right]M_w^{3.139} \tag{8}$$

$$\lambda_2 = 1.526 \cdot 10^{-13} \exp\left[\frac{E_\infty}{R}\left(\frac{1}{T} - \frac{1}{T_r}\right)\right] M_w^{1.351} \quad (9)$$

where T is the temperature in Kelvin, T_r is the reference temperature (equal to 503.15 K), E_0 and E_∞ are the zero and the infinite flow activation energies, R is the universal gas constant (8.314 J/K/mol).

Extensional rheology

The measured uniaxial extensional viscosity, $\eta_{E,U}$, is plotted as a function of the extensional strain rate, $\dot{\varepsilon}$, in Figure 5 (top) for all three linear isotactic polypropylene samples. As the strain rate increases, $\eta_{E,U}$ decreases, reaches the minimum value, $\eta_{E,U,min}$, (zone I) and then, it increases due to starting occurrence of the chain stretch (zone II) to the plateau value, $\eta_{E,U,\infty}$, which corresponds to the maximum chain stretch (zone III). The transition between zone I and zone II occurs at $\dot{\varepsilon} = \frac{1}{\lambda_S}$

where λ_S is the stretch relaxation time, which is estimated here by fitting of the measured data with a polynomial function (see Table 2). This behavior is consistent with predictions arising from the molecular based constitutive equations for linear polymer melts [50]. The measured extensional viscosity data can also be discussed in term of the dimensionless Weissenberg number, *Wi*, defined as the ratio of elastic to viscous forces (see Figure 5, bottom). In zone I, the chain orientation Weissenberg number $Wi_1 = \lambda_1 \dot{\varepsilon} >> 1$ (namely 10 - 300) but the chain stretch Weissenberg number $Wi_S = \lambda_S \dot{\varepsilon}$ is still small (<1), i.e. the maximum orientation of the primitive path of the molecule is reached but there is no stretching. The extensional stress becomes constant (or rises less than linearly with increased $\dot{\varepsilon}$) and hence extensional thinning occurs [41]. In zone II, when

$1 \le \mathrm{Wi_S} = \lambda_S \dot{\varepsilon} <$ about 7, the polymer molecules becomes fully aligned and stretched, leading to a rapid increase in extensional viscosity (extensional thickening). In zone III, when $\mathrm{Wi_S} = \lambda_S \dot{\varepsilon} >$ about 7, the maxim chain stretch is achieved, extensional stress increases linearly with increased $\dot{\varepsilon}$ and extensional viscosity becomes constant, equal to high-strain rate plateau, given by $\eta_{E,U,\infty}$. It can also be seen in Figure 5 that the decrease in M_w widens the region at $\eta_{E,U,min}$, where the extensional viscosity depends very weakly on the extensional strain rate and also increases Wi at which the maximum chain stretch is reached.

$\eta_{E,U,min}$ and $\eta_{E,U,\infty}$ are related to M_w in Figure 6 at T = T_r = 230 °C. It is obvious that both variables are linearly scaled with M_w in a log-log scale and $\eta_{E,U,\infty}$ shows a very weak dependence on M_w. The experimental data were fitted with power-law functions and the following relationships were found (considering that both variables have the same Arrhenius temperature dependence as η_∞).

$$\eta_{E,U,\infty} = 20.853 \exp\left[\frac{E_\infty}{R}\left(\frac{1}{T}-\frac{1}{T_r}\right)\right] M_w^{0.103} \tag{10}$$

$$\eta_{E,U,min} = 4.837 \cdot 10^{-7} \exp\left[\frac{E_\infty}{R}\left(\frac{1}{T}-\frac{1}{T_r}\right)\right] M_w^{1.580} \tag{11}$$

As can be seen, both variables decrease with decreased M_w or with increased temperature.

$\eta_{E,U}$ normalized by the three times zero-shear rate viscosity, η_0, plotted as a function of the extensional strain rate at T_0 = 230 °C, is shown in Figure 7 for all three samples tested. Very interestingly, samples with M_w equal to 76 and 64 kg/mol show extensional strain hardening (i.e. $\frac{\eta_{E,U}}{3\eta_0} > 1$) at very high extensional strain rates due to chain stretch, but sample with M_w equal to 56

kg/mol does not. Thus, there is a critical M_w below which extensional strain hardening starts to occur at very high extensional strain rates. Figure 8 shows the measured maximum extensional strain hardening, $\frac{\eta_{E,U,\infty}}{3\eta_0}$, plotted as a function of M_w at T = T_r = 230 °C. The measured data were successfully fitted with the following power-law equation considering that the temperature shift factor is the same as for the η_∞/η_0 ratio [9].

$$\frac{\eta_{E,U,\infty}}{3\eta_0} = \exp(39.524)\exp\left[\frac{E_\infty - E_0}{R}\left(\frac{1}{T}-\frac{1}{T_r}\right)\right]M_w^{-3.518} \quad (12)$$

Since the flow activation energies are not the same in the entangled as disentangled states, $\frac{\eta_{E,U,\infty}}{3\eta_0}$ depends not only on M_w, but also on the temperature. In more detail, $\frac{\eta_{E,U,\infty}}{3\eta_0}$ increases with decreased M_w and increased temperature, as can be seen from Eq.12 and its visualization in Figure 8.

Understanding of melt blowing process dynamics

SEM images, fiber diameter distributions, and log-normal function fits for produced nonwovens from linear isotactic polypropylenes are shown in Figs. 9 – 14. In order to understand the dynamics of the melt blowing process, λ_1, λ_2/λ_1 and $\frac{\eta_{E,U,\infty}}{3\eta_0}$ parameters were calculated for given temperatures and M_w of processed samples using Eqs. 8, 9, 12 and are summarized in Table 3. The same parameters were also determined for selected experimental data taken from the open literature for linear isotactic polypropylenes (see Table 4). The following three criteria were used

to select data from the open literature. First, the processing temperature (T_{die}) and M_w of the given PP are provided. Second, the average fiber diameters of produced fibers are comparable with those produced in this work. Third, *CV*, standard deviation or raw fiber diameter distribution data allowing the *CV* determination are given. In some studies, [10, 16, 51 – 56], M_w is provided only for pellets, not for processed samples. Therefore, the M_w of the processed samples was considered to be 12.5 % less than M_w of the polymer pellets during the calculation of λ_1, λ_2/λ_1 and $\frac{\eta_{E,U,\infty}}{3\eta_0}$ via Eqs. 8, 9, 12. The value of 12.5 % was calculated as the average reduction M_w of the polymer pellets at high strain rates (at $10^5 - 10^7$ 1/s, which are typical for the melt blowing process) and T_{die} = 230 °C (i.e. at a temperature which is the same as for the extensional viscosity measurements performed in this work) using the experimental data shown in Figure 13 in [57].

The *CV* plotted as a function of λ_1, λ_2/λ_1 and $\frac{\eta_{E,U,\infty}}{3\eta_0}$ is shown in the Figures 15 – 17 for all considered linear isotactic PPs summarized in the Tables 3 – 4. It can be seen that in general, *CV* decreases when λ_1 increases or when λ_2/λ_1 decreases due to increased M_w or decreased temperature, which is in good agreement with previous experimental reports [9, 15]. This general trend can be understood using the minimum uniaxial extensional viscosity, $\eta_{E,U,min}$, which shows a similar functional dependence on M_w and T as the parameters λ_1 and λ_2 (compare Eqs. 8, 9 and 11). $\eta_{E,U,min}$ can be viewed as a rheological parameter that controls stretching ability of the melt at extensional strain rates typical for the melt blowing process. Thus, increasing $\eta_{E,U,min}$ (by increasing M_w or decreasing T) helps to resist inhomogeneous stretching in the post-die area, which reduces *CV*. Of course, $\eta_{E,U,min}$ must be within a certain range, which allows stretching of the polymer melt to the desired fiber diameter. This is because if $\eta_{E,U,min}$ is too high, the melt-stretching ability is low, and the resulting fiber diameters are too high or $\eta_{E,U,min}$ is too low, and the fiber

breaks. However, there are certain specific cases where *CV* does not correlate with the λ_1 and λ_2/λ_1 variables (i.e. with $\eta_{E,U,min}$). These cases are clearly marked in Figs. 15 – 16. However, if the *CV* is plotted as a function of $\frac{\eta_{E,U,\infty}}{3\eta_0}$ (calculated via Eq.12), a clear functional dependence can be observed in all considered cases (see Figure 17). The following four specific regions can be identified. $\frac{\eta_{E,U,\infty}}{3\eta_0} \leq 1$, and $4 < \frac{\eta_{E,U,\infty}}{3\eta_0} \leq 5$, where the increase in $\frac{\eta_{E,U,\infty}}{3\eta_0}$ increases *CV*; $1 < \frac{\eta_{E,U,\infty}}{3\eta_0} \leq 4$ where the increase in $\frac{\eta_{E,U,\infty}}{3\eta_0}$ decreases *CV* and finally, $\frac{\eta_{E,U,\infty}}{3\eta_0} > 5$, where the increase in $\frac{\eta_{E,U,\infty}}{3\eta_0}$ has practically no effect on the *CV*. In the other words, there is a processing window given by $1 < \frac{\eta_{E,U,\infty}}{3\eta_0} \leq 4$, in which the *CV* is reduced by increasing $\frac{\eta_{E,U,\infty}}{3\eta_0}$ via reducing of M_w or by increasing the temperature (see Eq.12 and Figure 17). The observed trend can be understood from a molecular point of view through an increased monomeric friction coefficient, which enhances extensional thickening at very high extensional strain rates and suppresses capillary breakup [41]. The flow stability, here quantified by *CV*, can thus be fully understood by $\eta_{E,U,min}$ and $\frac{\eta_{E,U,\infty}}{3\eta_0}$ as follows. If $\eta_{E,U,min}$ is high and $\frac{\eta_{E,U,\infty}}{3\eta_0} < 1$ (Case I), the stabilizing effect of high $\eta_{E,U,min}$ dominates over destabilizing effect of no extensional strain hardening. If $\eta_{E,U,min}$ is low and $1 < \frac{\eta_{E,U,\infty}}{3\eta_0} \leq 4$ (Case II), the stabilizing effect of the present extensional strain hardening is higher than the destabilizing effect of low $\eta_{E,U,min}$. If $\eta_{E,U,min}$ is very low and $\frac{\eta_{E,U,\infty}}{3\eta_0} > 4$ (Case III), the destabilizing effect of low $\eta_{E,U,min}$ dominates over the stabilizing effect of high extensional strain hardening. As can be

seen from Eq.11 and Eq.12, $\eta_{E,U,min}$ and $\frac{\eta_{E,U,\infty}}{3\eta_0}$ depend on M_w and temperature, which allows visualization of all three cases graphically (see Figures 18 – 19). The critical boundaries visualized in these Figures are given by Eqs. 13 – 14 with $\frac{\eta_{E,U,\infty}}{3\eta_0}$ is equal 1 and 4 for transitions I/II and II/III. The first equation arises from Eq. 12, while the second from Eq.11 and Eq.13.

$$M_w = \left\{\left(\frac{\eta_{E,\infty}}{3\eta_{S,0}}\right)^{-1} \exp(39.524)\exp\left[\frac{E_\infty - E_0}{R}\left(\frac{1}{T}-\frac{1}{T_r}\right)\right]\right\}^{\frac{1}{3.518}} \quad (13)$$

$$\eta_{E,U,min} = 24.831\left(\frac{\eta_{E,\infty}}{3\eta_{S,0}}\right)^{-0.449} \exp\left[\frac{1.449E_\infty - 0.449E_0}{R}\left(\frac{1}{T}-\frac{1}{T_r}\right)\right] \quad (14)$$

Figures 18 – 19 and Eq.13 – 14 have very practical implications as they allow the selection of linear isotactic polypropylene (based on M_w or $\eta_{E,U,min}$) and processing temperature to minimize the non-uniformity of fibers produced, captured here via *CV*. The term "non-uniform" fibers refers to the width of the fiber diameter distribution, the pore size distribution and the structural anisotropy of the meltblown nonwoven fabrics. For example, in the field of filtration (i.e. for HVCA filters, HEPA filters, ULPA filters, medical face-mask, respiratory filters and dry and liquid aerosol filters), the presence of highly non-uniform fibers is intolerable because large fiber diameter changes lead to a wider pore size distribution and formation of more anisotropic structures, which reduces the mechanical and filtration properties of nonwovens [58, 59].

It is interesting to note that extensional thickening has been quite well studied in film blowing process for polyolefins and one could see a similarity with results obtained in this work for melt blowing process. In particular, the observation that there are optimal values for extensional thickening and melt strength with respect to the stability window size. The key difference seems

to be the mechanism in which the extensional thickening (i.e. the friction) is induced in both processes, because the strain rates are very different. At low strain rates, which are typical for film blowing process (i.e. when the flow starts to orient the primitive path of the molecules), stabilizing extensional thickening can be induced by adding long side branches to the polymer [60]. However, at very high extensional strain rates, which are typical for the melt blowing process (i.e. when chain stretch occurs), extensional thickening can occur even for linear polymers, as long as the coefficient of friction remains high enough. Thus, it can be expected that different monomer chemistries can be used to control high extensional rheology by varying the friction coefficient at very high extensional rates to stabilize the melt blowing process considerably.

CONCLUSION

In this work, three linear isotactic polypropylenes having different M_w (56, 64 and 76 kg/mol) and a comparable polydispersity M_w/M_n (3.95 – 4.41) were used for the production of nonwovens by melt blowing technology at two different temperatures (250 ^oC and 270 ^oC) in order to understand role of M_w and T on the fiber diameter distribution. Melt elasticity was evaluated using the reptation-mode relaxation time, λ_1, and the Rouse-mode reorientation time, λ_2, determined from shear viscosity data covering a very wide range of shear rate (10 – 10^7 1/s). Extensional rheology was assessed by the strain rate dependent uniaxial extensional viscosity (estimated from the entrance pressure drop using the Gibson method). Obtained plateau value of uniaxial extensional viscosity at the highest extensional strain rates, $\eta_{E,\infty}$, (normalized by the three times zero-shear rate viscosity, η_0) and the minimum uniaxial extensional viscosity, $\eta_{E,U,min}$ were related to M_w and T using simple analytical equations. The basic morphological characteristics of the produced

nonwoven samples were determined by digital image analysis of SEM images considering three different magnifications for the capture of nanofibers and microfibers. The obtained data were combined with relevant literature data for linear isotactic polypropylenes having the M_w between 26 – 224 kg/mol processed by the melt blowing technology over a wide temperature range (180 – 260 °C).

It has been found that firstly, the chosen reptation-mode relaxation time, λ_1, and the Rouse-mode reorientation time, λ_2, show (in the power-law dependency with M_w) a slope of about 3.14 and 1.35, respectively, indicating that λ_1 and λ_2 characterize elasticity of the melt in highly entangled and almost disentangled states. Second, the extensional viscosity for all three samples decreases with increasing extensional strain rate to its minimum value, $\eta_{E,U,min}$, at 20 000 – 200 000 1/s, and then increases to plateau value, $\eta_{E,\infty}$ at approximately 2×10^6 1/s. Third, the decrease in M_w widens the region at $\eta_{E,U,min}$, where the extensional viscosity depends very weakly on the extensional strain rate. Fourth, $\eta_{E,U,min}$ shows a slope of 1.58 in the power-law dependency with M_w (which is comparable to the value of 1.35 for λ_2), but the dependence of $\eta_{E,U,\infty}$ on M_w was found to be very weak, as deduced from very low power-law exponent - equal to 0.1. Fifth, there is a critical M_w, below which the extensional strain hardening starts to occur at very high strain rates ($\frac{\eta_{E,U,\infty}}{3\eta_0}>1$). $\frac{\eta_{E,U,\infty}}{3\eta_0}$ was related to M_w and temperature using a simple power-law equation. Interestingly, $\frac{\eta_{E,U,\infty}}{3\eta_0}$ was found to be inversely proportional to M_w and temperature. Finally, it was shown that the stability of fibers production captured by *CV* is complex, depending exclusively on the extensional properties of polypropylene melts, namely $\frac{\eta_{E,U,\infty}}{3\eta_0}$ and $\eta_{E,U,min}$. The existence of optimal conditions under which the *CV* is minimal was attributed to the opposite trends of these

two parameters with M_w and T. Simple mathematical formulas were provided to determine these optimum conditions.

The current understanding for linear isotactic PP melts was that decreased M_w or increased T (i.e. decreased λ_1 or increased λ_2/λ_1) increases CV [9, 15]. This work has shown that this trend is valid only in a certain range of M_w and T (i.e. in zone I and III in Figures 18 – 19) and that there are process conditions in which a decrease in M_w (or increase in T) can significantly reduce CV (zone II in Figures 18 – 19) due to the extensional strain hardening, which begins to appear at very high extensional strain rates (i.e. if $1 < \frac{\eta_{E,U,\infty}}{3\eta_0} \leq 4$). Since the optimal value for $\frac{\eta_{E,U,\infty}}{3\eta_0}$ was found to be about 4, one can use Eq. 13 to determine the lowest possible M_w (for a given temperature), at which the CV is considerably minimized. These findings are particularly important with respect to the stable production of polymeric nanofibers by melt blowing technology, in which low molecular weight polymers and high temperatures are needed to reduce the fiber diameter to the desired level.

SUPPLEMENTARY MATERIAL

See supplementary material for further details on the determination of average fiber diameter and coefficient of variation from digitized histograms taken from the open literature.

ACKNOWLEDGMENTS

The authors would like to acknowledge the Institutional Support Project 2020 (Polymer Centre at Faculty of Technology, Tomas Bata University in Zlin). The authors also wish to acknowledge Joachim Fiebig from Borealis Polyolefine (Linz, Austria) for donation of the polypropylene meltblown samples, help with the GPC measurements and to allowing us to perform all melt blowing experiments as well as scanning electron microscopy on Borealis Polyolefine laboratory equipment.

DATA AVAILABILITY

The data that supports the findings of this study are available within the article [and its supplementary material].

REFERENCES

[1] NAYAK, R., I. L. KYRATZIS, Y. B. TRUONG, R. PADHYE, L. ARNOLD, G. PEETERS, M. O'SHEA and L. NICHOLS, Fabrication and characterization of polypropylene nanofibres by meltblowing process using different fluids. Journal of Materials Science. 2013, vol. 48, no. 1, p. 273 – 281.

[2] DUTTON, K. C., Overview and analysis of the meltblown process and parameters. Journal of Textile and Apparel, Technology and Management. 2009, vol. 6, no. 1., p. 1 – 24

[3] DAS, D., A. K. PRADHAN, R. CHATTOPADHYAY and S. N. SINGH, Composite nonwovens. Textile Progress. 2012, vol. 44, no. 1, p. 1 – 84.

[4] PU, Y., J. ZHENG, F. CHEN, Y. LONG, H. WU, Q. LI, S. YU, X. WANG and X. NING, Preparation of polypropylene micro and nanofibers by electrostatic-assisted melt blown and their application. Polymers. 2018, vol. 10, Article number 959.

[5] BRESEE, R. R. and W. KO., Fiber formation during melt blowing. International Nonwovens Journal. 2003, vol. 12, no. 2, p. 21 – 28.

[6] DE ROVERE, A., R. L. SHAMBAUGH and E. A. O'REAR, Investigation of gravity-spun, melt-spun, and melt-blown polypropylene fibers using atomic force microscopy. Journal of Applied Polymer Science. 2000, vol. 77, no. 9, p. 1921 – 1937.

[7] HUTTEN, I. M., Processes for Nonwoven Filter Media. In: Handbook of Nonwoven Filter Media, Second Edition, Butterworth-Heinemann. Kidlington, UK, 2015, 276-342. ISBN 978-0-08-098301-1

[8] KARTHIK, T., C. PRABHA KARAN, R. RATHINAMOORTHY, Non-woven: Process, Structure, Properties and Applications, Woodhead Publishing India in Textiles. CRC Press, 2016, p. 358. ISBN 978-9385059124

[9] DRABEK, J. and M. ZATLOUKAL, Influence of long chain branching on fiber diameter distribution for polypropylene nonwovens produced by melt blown process. Journal of Rheology. 2019, vol. 63, no. 4, p. 519 – 532.

[10] ELLISON, C. J., A. PHATAK, D. W. GILES, C. W. MACOSKO and F. S. BATES, Melt blown nanofibers: fiber diameter distributions and onset of fiber breakup. Polymer. 2007, vol. 48, no. 11, p. 3306 – 3316.

[11] RAO, R. S. and R. L. SHAMBAUGH, Vibration and stability in the melt blowing process. Industrial and Engineering Chemistry Research. 1993, vol. 32, no. 12, p. 3100 – 3111.

[12] CHEN, T., C. ZHANG, X. CHEN and Q. LI, Numerical computation of the fiber diameter of melt blown nonwovens produced by the inset die. Journal of Applied Polymer Science. 2009, vol. 111, no. 4, p. 1775 – 1779.

[13] XIE, S. and Y. C. ZENG, A geometry method for calculating the fiber diameter reduction in melt blowing. Advanced Materials Research. 2014, vol. 893, p. 87 – 90.

[14] XIE, S., Y. ZHENG, and Y. ZENG, Influence of die geometry on fiber motion and fiber attenuation in the melt-blowing process. Industrial and Engineering Chemistry Research. 2014, vol. 53, no. 32, p. 12866 – 12871.

[15] TAN, D. H., C. ZHOU, C. J. ELLISON, S. KUMAR, C. W. MACOSKO and F. S. BATES, Meltblown fibers: influence of viscosity and elasticity on diameter distribution. Journal of Non-Newtonian Fluid Mechanics. 2010, vol. 165, no. 15-16, p. 892 – 900.

[16] HASSAN, M. A., B. Y. YEOM, A. WILKIE, B. POURDEYHIMI and S. A. KHAN, Fabrication of nanofiber meltblown membranes and their filtration properties. Journal of Membrane Science. 2013, vol. 427, p. 336 – 344.

[17] SHAMBAUGH, R. L., A macroscopic view of the melt-blowing process for producing microfibers. Industrials and Engineering Chemistry Research. 1988, vol. 27, no. 12, p. 2363 – 2372.

[18] WARD, G. F., Meltblown nanofibers for nonwoven filtration applications. Filtration and Separation. 2001, vol. 38, no. 9, p. 42 – 43.

[19] HAN, W., X. WANG and G. S. BHAT, Structure and air permeability of melt blown nanofiber webs, Journal of Nanomaterials & Molecular Nanotechnology. 2013, vol. 2, no. 3.

[20] WANG, Z., X. LIU, C. W. MACOSKO and F. S. BATES, Nanofibers from water-extractable melt-blown immiscible polymer blends. Polymer (United Kingdom). 2016, vol. 101, p. 269 – 273.

[21] SOLTANI, I. and C. W. MACOSKO, Influence of rheology and surface properties on morphology of nanofibers derived from islands-in-the-sea meltblown nonwovens. Polymer (United Kingdom). 2018, vol. 145, p. 21 – 30.

[22] ZUO, F., D. H. TAN, Z. WANG, S. JEUNG, C. W. MACOSKO and F. S. BATES, Nanofibers from melt blown fiber-in-fiber polymer blends. ACS Macro Letters. 2013, vol. 2, no. 4, p. 301 – 305.

[23] HAO, X. and Y. ZENG, A review on the studies of air flow field and fiber formation process during melt blowing. Industrial and Engineering Chemistry Research. 2019, vol. 58, no. 27, p. 11624 – 11637.

[24] MUSIL, J. and M. ZATLOUKAL, Historical review of die drool phenomenon in plastics extrusion. Polymer Reviews. 2014, vol. 54, no. 1, p. 139 – 184.

[25] MUSIL, J. and M. ZATLOUKAL, Effect of die exit geometry on internal die drool phenomenon during linear HDPE melt extrusion. International Journal of Heat and Mass Transfer. 2013, vol. 56, no. 1 – 2, p. 667 – 673.

[26] MUSIL, J. and M. ZATLOUKAL, Experimental investigation of flow induced molecular weight fractionation phenomenon for two linear HDPE polymer melts having same M_n and M_w but different M_z and M_{z+1} average molecular weights. Chemical Engineering Science. 2012, vol. 81, p. 146 – 156.

[27] MUSIL, J. and M. ZATLOUKAL, Experimental investigation of flow induced molecular weight fractionation during extrusion of HDPE polymer melts. Chemical Engineering Science. 2011, vol. 66, no. 20, 4814 – 4823.

[28] MUSIL, J. and M. ZATLOUKAL, Investigation of die drool phenomenon for HDPE polymer melt. Chemical Engineering Science. 2010, vol. 65, no. 23, p. 6128 – 6133.

[29] CHALOUPKOVA, K. and M. ZATLOUKAL, Effect of die design on die drool phenomenon for metallocene based LLDPE: Theoretical and experimental investigation. Journal of Applied Polymer Science. 2009, vol. 111, no. 4, 1728 – 1737.

[30] CHALOUPKOVA, K. and M. ZATLOUKAL, Theoretical and experimental analysis of the die drool phenomenon for metallocene LLDPE. Polymer Engineering and Science. 2007, vol. 47, no. 6, 871 – 881.

[31] KONAGANTI, V. K., M. DERAKHSHANDEH, M. EBRAHIMI, E. MITSOULIS and S. G. HATZIKIRIAKOS, Non-isothermal extrudate swell. Physics of Fluids. 2016, vol. 28, no. 12, Article number 123101.

[32] TOUKHTARIAN, R., S. G. HATZIKIRIAKOS, H. ATSBHA and B. BOULET, Modeling polymer extrusion with varying die gap using Arbitrary Lagrangian Eulerian (ALE) method. Physics of Fluids. 2018, vol. 30, no. 9, Article number 093103.

[33] EVANS, J. D. and M. L. EVANS, The extrudate swell singularity of Phan-Thien-Tanner and Giesekus fluids. Physics of Fluids. 2019, vol. 31, no. 11, Article number 5129664.

[34] TANG, D., F. H. MARCHESINI, L. CARDON and D. R. D'HOOGE, Three-dimensional flow simulations for polymer extrudate swell out of slit dies from low to high aspect ratios. Physics of Fluids. 2019, vol. 31, no. 9, Article number 93103.

[35] BARBORIK, T. and M. ZATLOUKAL, Steady-state modeling of extrusion cast film process, neck-in phenomenon, and related experimental research: A review. Physics of Fluids. 2020, vol. 32, Article number 061302.

[36] TANG, D., F. H. MARCHESINI, L. CARDON and D. R. D'HOOGE, The impact of upstream contraction flow on three-dimensional polymer extrudate swell from slit dies. Journal of Non-Newtonian Fluid Mechanics. 2020, vol. 282, Article number 104337.

[37] MUSIL, J. and M. ZATLOUKAL, Historical Review of Secondary Entry Flows in Polymer Melt Extrusion. Polymer Reviews. 2019, vol. 59, no. 2, p. 338 – 390.

[38] FERRAS, L. L., A. M. AFONSO, M. A. ALVES, J. M. NOBREGA and F. T. PINHO, Newtonian and viscoelastic fluid flows through an abrupt 1:4 expansion with slip boundary conditions. Physics of Fluids. 2020, vol. 32, Article number 043103.

[39] TOMKOVIC, T., E. MITSOULIS and S. G. HATZIKIRIAKOS, Contraction flow of ionomers and their corresponding copolymers: Ionic and hydrogen bonding effects. Physics of Fluids. 2019, vol. 31, no. 3, Article number 033102.

[40] DRABEK, J. and M. ZATLOUKAL, Meltblown technology for production of polymeric microfibers/nanofibers: A review. Physics of Fluids. 2019, vol. 31, no. 9, Article number 091301.

[41] LARSON, R. G. and P. S. DESAI, Modeling the rheology of polymer melts and solutions. Annual Review of Fluid Mechanics. 2015, vol. 47, p. 47 – 65.

[42] DRABEK, J., M. ZATLOUKAL and M. MARTYN, Effect of molecular weight on secondary Newtonian plateau at high shear rates for linear isotactic melt blown polypropylenes. Journal of Non-Newtonian Fluid Mechanics. 2018, vol. 215, p. 107 – 118.

[43] DRABEK, J., M. ZATLOUKAL and M. MARTYN, Effect of molecular weight, branching and temperature on dynamics of polypropylene melts at very high shear rates. Polymer. 2018, vol. 144, p. 179 – 183.

[44] GIBSON, A. G., Die entry flow of reinforced polymers. Composites. 1989, vol. 20, no. 1, p. 57 – 64.

[45] ZATLOUKAL, M., J. VLCEK, C. TZOGANAKIS, P. SAHA, Improvement in techniques for the determination of extensional rheological data from entrance flows: computational and experimental analysis. Journal of Non-Newtonian Fluid Mechanics. 2002, vol. 107, n. 1 – 3, p. 13 – 37.

[46] ZATLOUKAL, M., J. MUSIL, Analysis of entrance pressure drop techniques for extensional viscosity determination. Polymer Testing. 2009, vol. 28, no. 8, p. 843 – 853.

[47] SAMBAER, W., M. ZATLOUKAL, D. KIMMER, 3D modeling of filtration process via polyurethane nanofiber based nonwoven filters prepared by electrospinning process. Chemical Engineering Science. 2011, vol. 66, no. 4, p. 613 – 623.

[48] SAMBAER, W., M. ZATLOUKAL, D. KIMMER, 3D air filtration modeling for nanofiber based filters in the ultrafine particle size range. Chemical Engineering Science. 2012, vol. 82, p. 299 – 311.

[49] LIMPERT, E., W. A. STAHEL, M. ABBT, Log-normal distributions across the sciences: keys and clues, BioScience. 2001, vol. 51, no. 5, p. 341 – 352.

[50] DELAY, J. M., D. J. READ, R. G. LARSON, Structure and rheology of molten polymers: from structure to flow behavior and back again, 2nd edition, Cincinnati, Hanser, 2018, p. 610, ISBN: 9781569906118.

[51] SHIM, W. S., D. W. LEE, Quality variables of meltblown submicron filter materials. Indian Journal of Fiber and Textile Research. 2013, vol. 38, no. 2, p. 132 – 137.

[52] UPPAL, R., G. BHAT, C. EASH and K. AKATO, Meltblown nanofiber media for enhanced quality factor. Fibers and Polymers. 2013, vol. 14, no. 4, p. 660 – 668.

[53] KHAN, A. Y. A., A fundamental investigation of the effects of die geometry and process variables on fiber diameter and quality of melt blown polypropylene webs. Ph.D Thesis. The University of Tennessee, Knoxville, USA, 1993.

[54] LI, H., H. HUANG and Y. ZENG, Effects of compatibilizer and airflow field on the formation of helical microfibers via melt blowing. Journal of Polymer Science, Part B: Polymer Physics. 2019, vol. 57, no. 21, p. 1423 – 1433.

[55] RUNGIAH, S., R. RUAMSUK, P. VROMAN, W. TAKARADA, J. C. APPERT-COLLIN and T. KIKUTANI, Structural characterization of polypropylene/poly(lactic acid) bicomponent meltblown. Journal of Applied Polymer Science. 2017, vol. 134, no. 14, Article number 44540.

[56] HAN, W., G. S. BHAT and X. WANG, Investigation of nanofiber breakup in the melt-blowing process. Industrial and Engineering Chemistry Research. 2016, vol. 55, no. 11, p. 3150 – 3156.

[57] TAKAHASHI, H., T. MATSUOKA and T. KURAUCHI, Rheology of polymer melts in high shear rate. Journal of Applied Polymer Science. 1985, vol. 30, no. 12, p. 4669 – 4684.

[58] SAMBAER, W., M. ZATLOUKAL, D. KIMMER, The use of novel digital image analysis technique and rheological tools to characterize nanofiber nonwovens. Polymer Testing. 2010, vol. 29, no. 1, p. 82 – 94.

[59] CAI, R. R., H. LU, L. Z. ZHANG, Evaluation the effect of fiber alignment on particle collection performance of mechanical/electret filters based on Voronoi tessellations. Chemical Engineering Science. 2019, vol. 197, p. 109 – 119.

[60] KOLARIK, R., M. ZATLOUKAL and M. MARTYN, The effect of polyolefin extensional rheology on non-isothermal film blowing process stability. International Journal of Heat and Mass Transfer. 2013, vol. 56, no. 1 – 2, p. 694 – 708.

[61] NAYAK, R., Polypropylene nanofibers: Melt electrospinning versus meltblowing. Springer. Engineering Materials, 2017, p. 190. ISBN 978-3-319-61457-1.

[62] BUTIN, R. R., J. P. KELLER and J. W. HARDING, Non-woven mats by melt blowing, US Patent US-3849241A (19 November 1974).

[63] BRANG, J., A. WILKIE and J. HAGGARD, Method and apparatus for production of meltblown nanofibers, US Patent US-2008023888-A1 (31 January 2008).

TABLE 1 Basic characteristics of used linear isotactic polypropylene melts (processed samples) taken from [42, 43].

Sample Name	M_n (g/mol)	M_w (g/mol)	M_z (g/mol)	M_{z+1} (g/mol)	M_w/M_n (-)	η_0 (Pa·s) T= 230 °C	η_∞ (Pa·s) T= 230 °C	E_0 (kJ/mol)	E_∞ (kJ/mol)
HL504FB	17200	75850	165500	278000	4.41	22.80	0.229	56.590	25.204
HL508FB	14650	63750	138000	235500	4.35	11.27	0.199		
HL512FB	14250	56250	114500	187500	3.95	7.79	0.165		

TABLE 2 Rheological parameters determined from shear (λ_1, λ_2, n) and uniaxial extensional viscositites (λ_S, $\eta_{E,min}$, $\eta_{E,U,\infty}/(3\eta_0)$) measured over a very wide rate range of strain rates for linear isotactic polypropylenes at 230 °C.

Sample Name	λ_1 (ms)	λ_2 (μs)	n (-)	λ_S (μs)	$\eta_{E,U,min}$ (Pa·s)	$\eta_{E,U,\infty}/(3\eta_0)$ (-)
HL504FB	1.201923	0.585	0.3964	4.123	24.95	0.9898
HL508FB	0.706714	0.491	0.4445	4.600	18.95	1.8243
HL512FB	0.469484	0.388	0.4569	5.005	15.55	2.8337

TABLE 3 Basic rheological characteristics shifted to the meltblown processing temperature via Arrhenius shift factor together with the corresponding coefficient of variation and air volume flow rate to achieve an average fiber diameter about 1.5μm. The processing conditions were as follows: orifice diameter: 0.4 mm; number of holes per active part: 470; collector belt speed: 5 m/min, die-to-collector distances: 500 mm; mass flow rate for one orifice: 0.0885 g/hole/min.

Material	T_{Die} (°C)	λ_1 (s)	λ_2/λ_1 (-)	$\eta_{E,U,\infty}/(3\eta_0)$ (-)	CV (%)	Standard deviation (%)	Air volume flow rate (m^3/hod)
PP Borflow HL504FB	250	0.0007197	0.0006571	1.3186371	55.35	1.4000	520
	270	0.0004457	0.0008571	1.7199753	54.85	1.3450	410
PP Borflow HL508FB	250	0.0004171	0.0008966	2.4303743	54.72	0.6400	400
	270	0.0002583	0.0011695	3.1700790	51.56	1.9250	320
PP Borflow HL512FB	250	0.0002816	0.0011215	3.7750415	44.88	0.7400	340
	270	0.0001744	0.0014629	4.9240070	60.31	2.3850	250

TABLE 4 Summary of basic rheological characteristics shifted to the meltblown processing temperature via the Arrhenius shift factor together with the average fiber diameter, the corresponding coefficient of variation and given meltblown processing conditions for linear isotactic polypropylenes, which are taken from the open literature.

Material	T_{Die} (°C)	M_w (g/mol)	λ_1 (s)	λ_2/λ_1 (-)	$\eta_{E,U,\infty}/(3\eta_0)$ (-)	D_{Fiber} (μm)	CV (%)	CV_{AV} (%)	Standard deviation (%)	DCD (mm)	Throughput (gram/hole/min)	D_{Die} (mm)	Notes (-)	Reference
PP	240	224 000**	0.018256517	0.000104533	0.040592104	0.570	37	27.83	6.600	250	0.022	0.1254	-	51, 52
						0.560	21			300				
						0.550	31			350				
						0.590	19			300			70+	
						0.560	21						100+	
						0.520	38						140+	
PP PD3495G	260	110 000**	0.001190822	0.000491386	0.653056944	1.980	33.71	31.51	2.205	305	0.8	0.381	Setback Face gap	53
						1.900	29.30				1.2			
PP DAELIM	240	103 000**	0.001593351	0.000419407	0.624548899	1.2-1.5 [c]	57.17	57.17	-	150	-	0.5		54
PP HL512FB	242	90950**	0.001024086	0.000539099	0.995593645	1.067 [d]	46.71 [d]	46.71	-	80	0.03	0.125	Air flow 300 m^3/hod	55
PP Exxon 3746G	220	59 000**	0.00047464	0.000842943	3.291381832	0.300	19.89	19.89	-	550	0.035	0.2	L/D = 10	10
PP Exxon, Achieve™ 6936G	230	60 000**	0.000380313	0.000952401	3.612198141	0.780	29.08 [e]	31.81	2.730	250	0.025	0.1254	AGR die	56
						0.810	34.54 [e]					0.01778	HILL die	
PP Exxon, Achieve™ 6936G	240	60 000**	0.00029218	0.001102349	4.180909757	0.636 [f]	5.71 [f]	6.55	1.241	190	0.025	0.178	-	16
						0.867 [f]	8.30 [f]				0.050			
						1.153 [f]	5.64 [f]				0.1			
PP*	200	41 564***	0.000430758	0.000898719	5.10594663	0.767 [g]	75.40 [g]	72.08	3.321	400	1.33	0.5	Water 5 [a]	61
						0.913 [g]	68.76 [g]			200				
PP*	200	40 875***	0.000408739	0.000925989	5.41524221	0.634 [g]	79.41 [g]	75.46	3.439	200			Water 10 [a]	
						0.632 [g]	71.02 [g]			300				
						0.570 [g]	75.95 [g]			400				
PP*	190	33 945***	0.000311233	0.001086607	8.76332668	0.620 [g]	69.97 [g]	68.98	0.983	300			Water 10 [a]	
						0.609 [g]	68.00 [g]			400				
PP*	190	33 708***	0.000304463	0.001100307	8.98203401	0.483 [g]	73.45 [g]	72.47	0.978	200			Water 5 [a]	
						0.430 [g]	71.50 [g]			400				
PP*	190	30 901***	0.000231744	0.001285405	12.1963166	0.797 [g]	71.98 [g]	75.24	2.729	200			Nitrogen 10 [b]	
						0.743 [g]	78.65 [g]			300				
						0.728 [g]	75.08 [g]			400				
PP*	190	29 703***	0.000204694	0.001379586	14.0167182	0.838 [g]	84.24 [g]	80.14	2.952	200			Air 10 [b]	
						0.793 [g]	78.79 [g]			300				
						0.736 [g]	77.40 [g]			400				
PP*	180	27 065***	0.000211429	0.001361019	16.2421239	0.725 [g]	63.99 [g]	66.85	2.624	200			Nitrogen 10 [b]	
						0.670 [g]	66.22 [g]			300				
						0.622 [g]	70.33 [g]			400				
PP*	180	26 158***	0.000189976	0.001446561	18.3116090	0.699 [g]	66.12 [g]	69.28	3.159	300			Air 10 [b]	
						0.631 [g]	72.44 [g]			400				

* PP were synthesized by the chain scission of the base polymer (Moplen 241R with a MFI of 30 from Lyondellbasell) using radical initiator (combination of 2, 5 dimethyl hexane and 2, 5 bis(tert-butyl peroxide) commonly known as DHBP.

** M_w values for polymer pellets

*** M_w values for processed samples

\+ Airflow pressure (kPa)

a ml/min

b g/min

c taken from the histogram visualized in Figure 9 (a) in [53]

d digitized from the histogram visualized in Figure 7 (b) in [54] (see supplementary material [45])

e digitized from the histogram visualized in Figure 6 in [55] (see supplementary material [45])
f taken from the Figure 3 in [16]
g taken from the Figure 8.13 in [59]

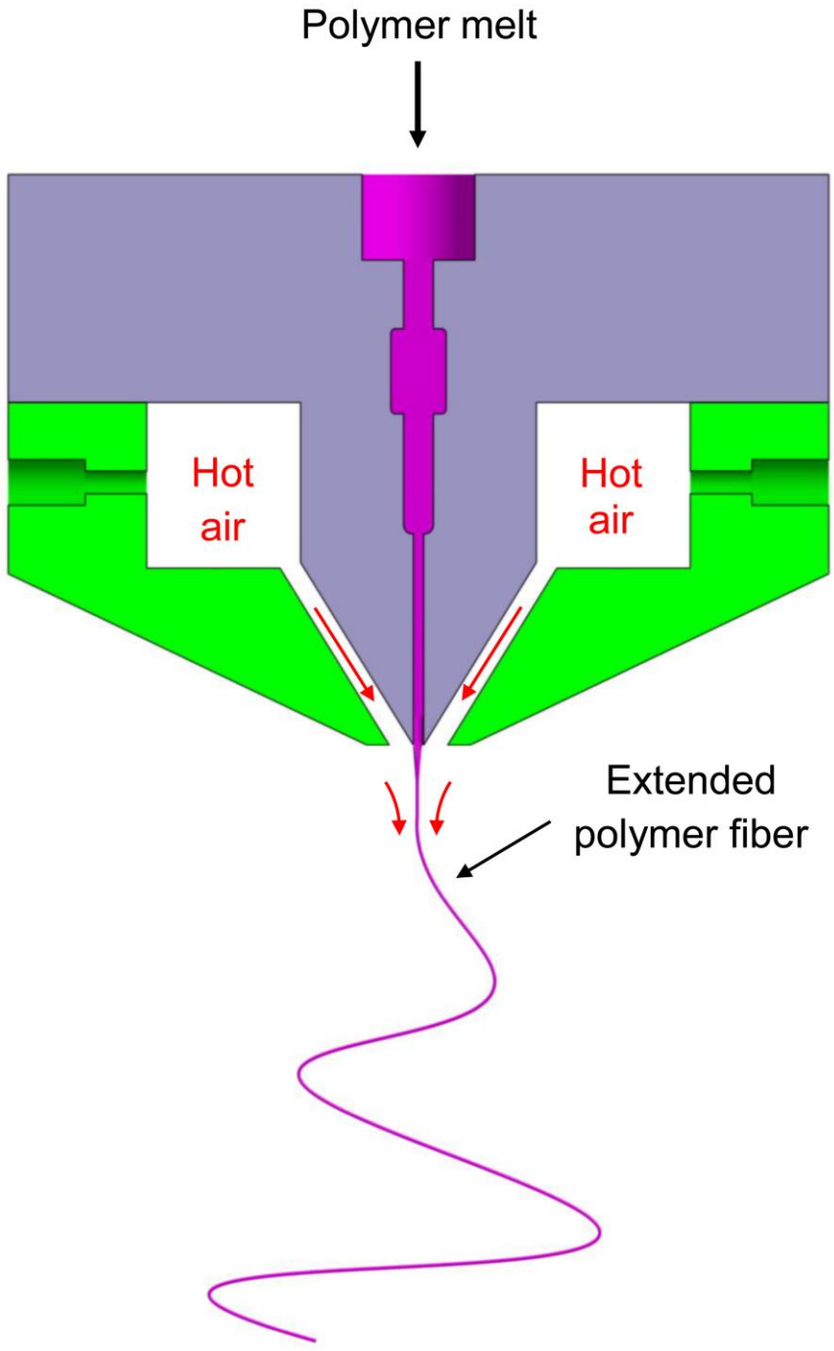

Figure 1 Scheme of the meltblown process. [62, 63]

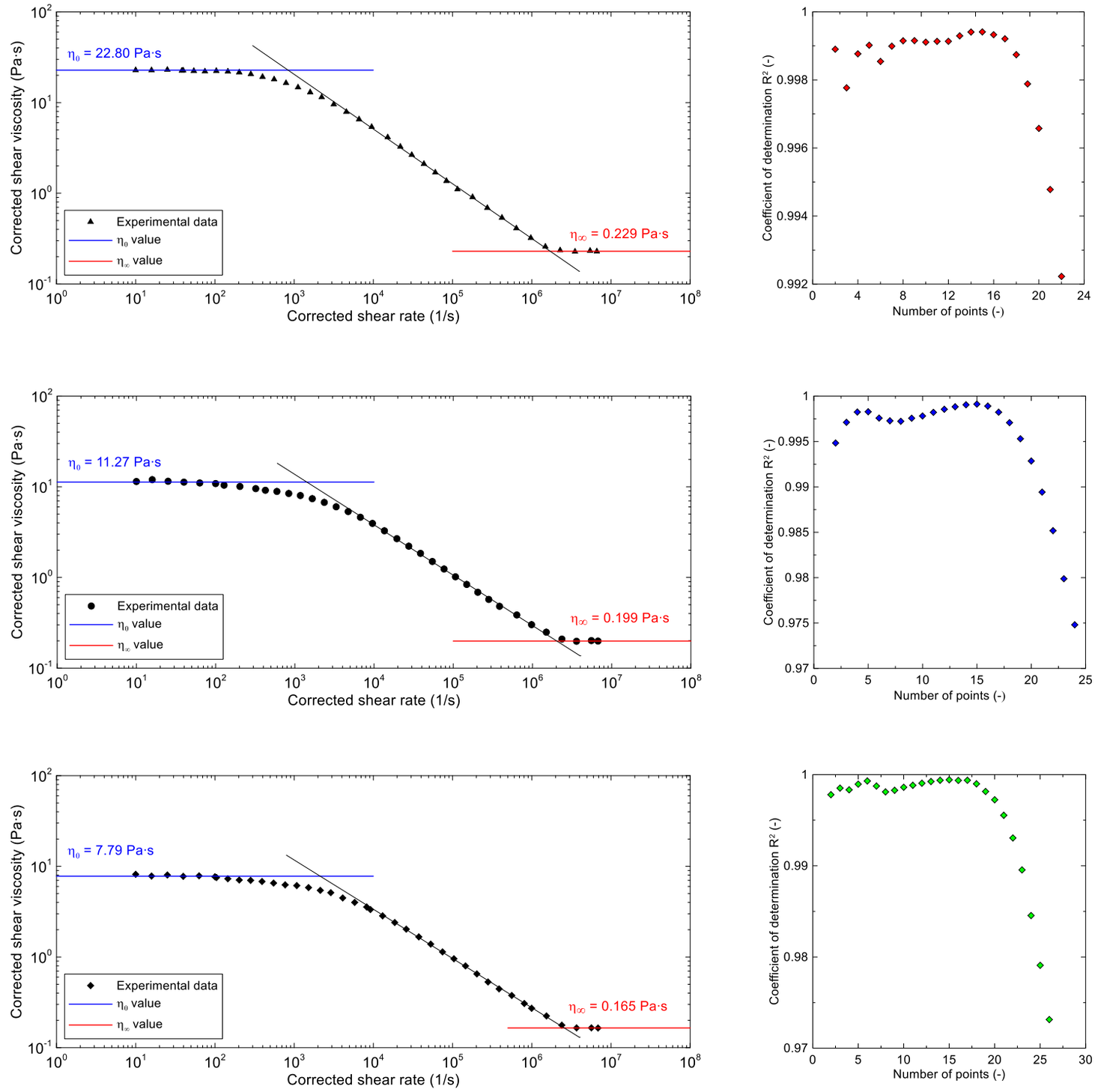

Figure 2 Determination of the reptation-mode relaxation time, λ_1, and the Rouse-mode reorientation time, λ_2, at 230 °C for three linear isotactic polypropylenes with M_w = 76 kg/mol (top), M_w = 64 kg/mol (middle) and M_w = 56 kg/mol (bottom). The corresponding coefficient of determination, R^2, for the power-law model used to fit the different number of points in the pseudoplastic region is shown on the right. Experimental data taken from [42].

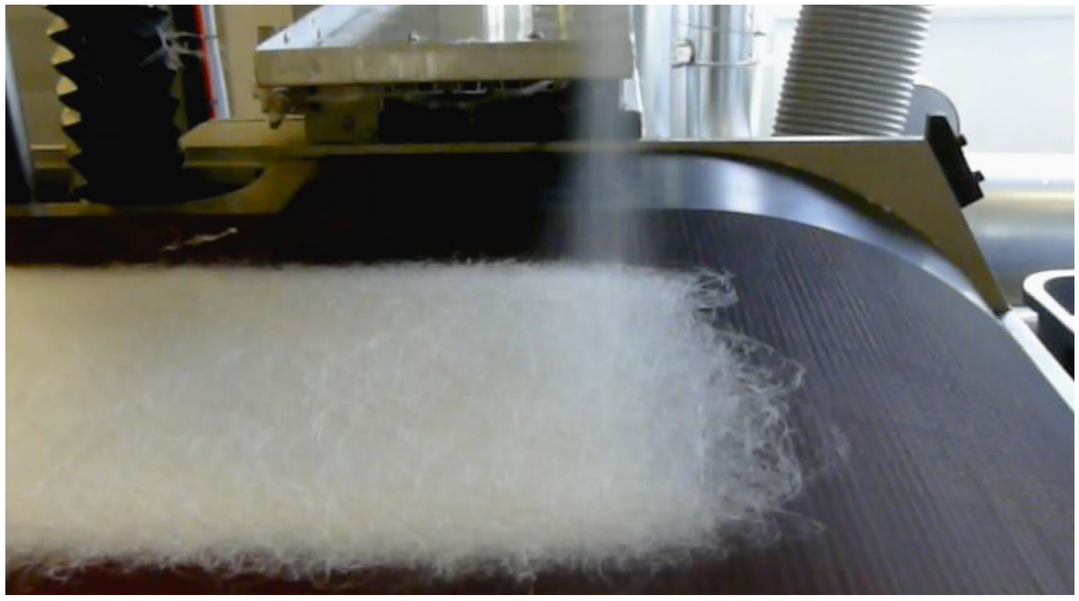

Figure 3 Reifenhäuser Reicofil pilot plant meltblown line (top - general view, bottom - Multimedia view).

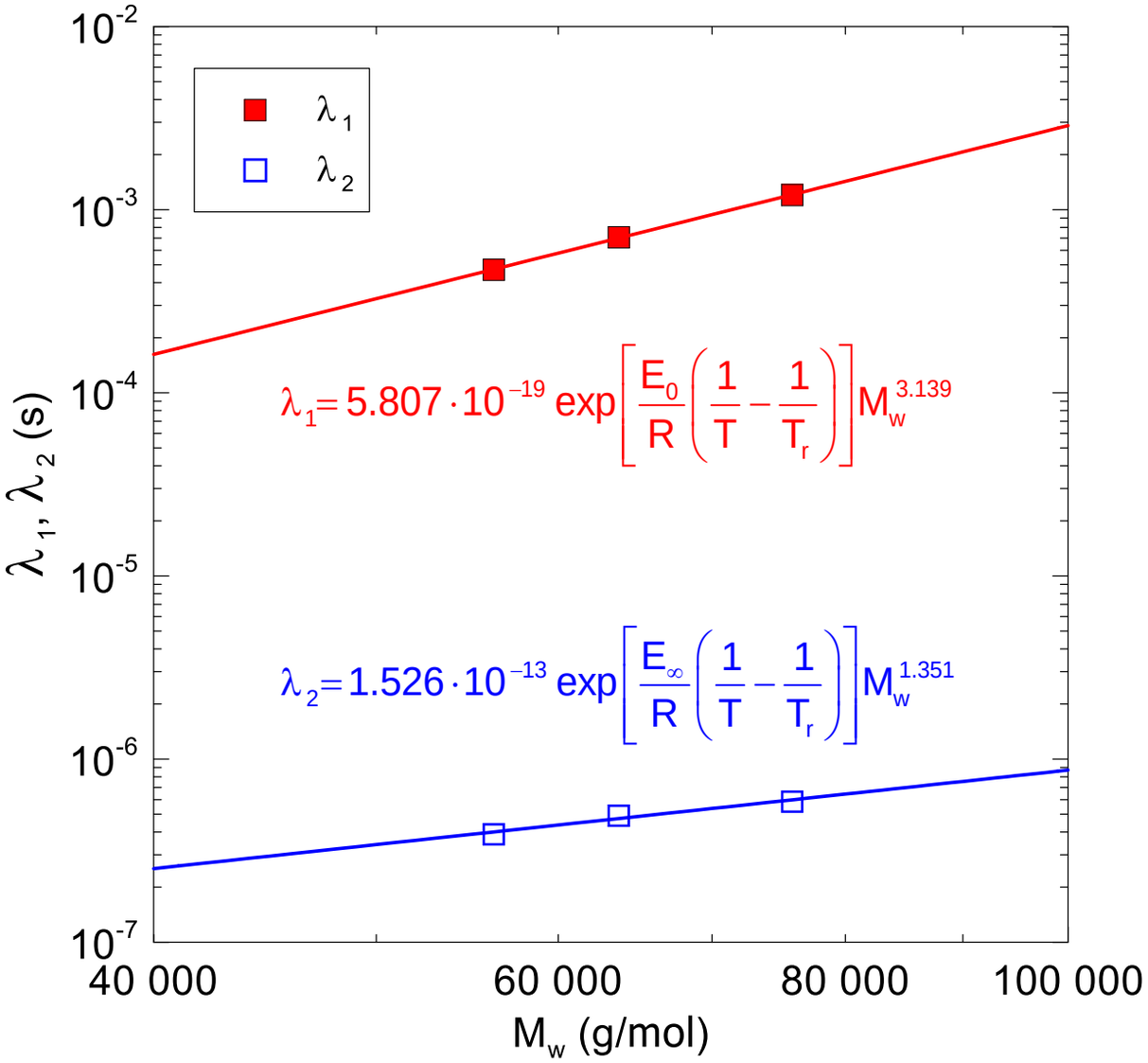

Figure 4 Reptation-mode relaxation time, λ_1, and Rouse-mode reorientation time, λ_2, plotted as a function of weight-average molecular weight, M_w, for linear isotactic polypropylene at 230 °C.

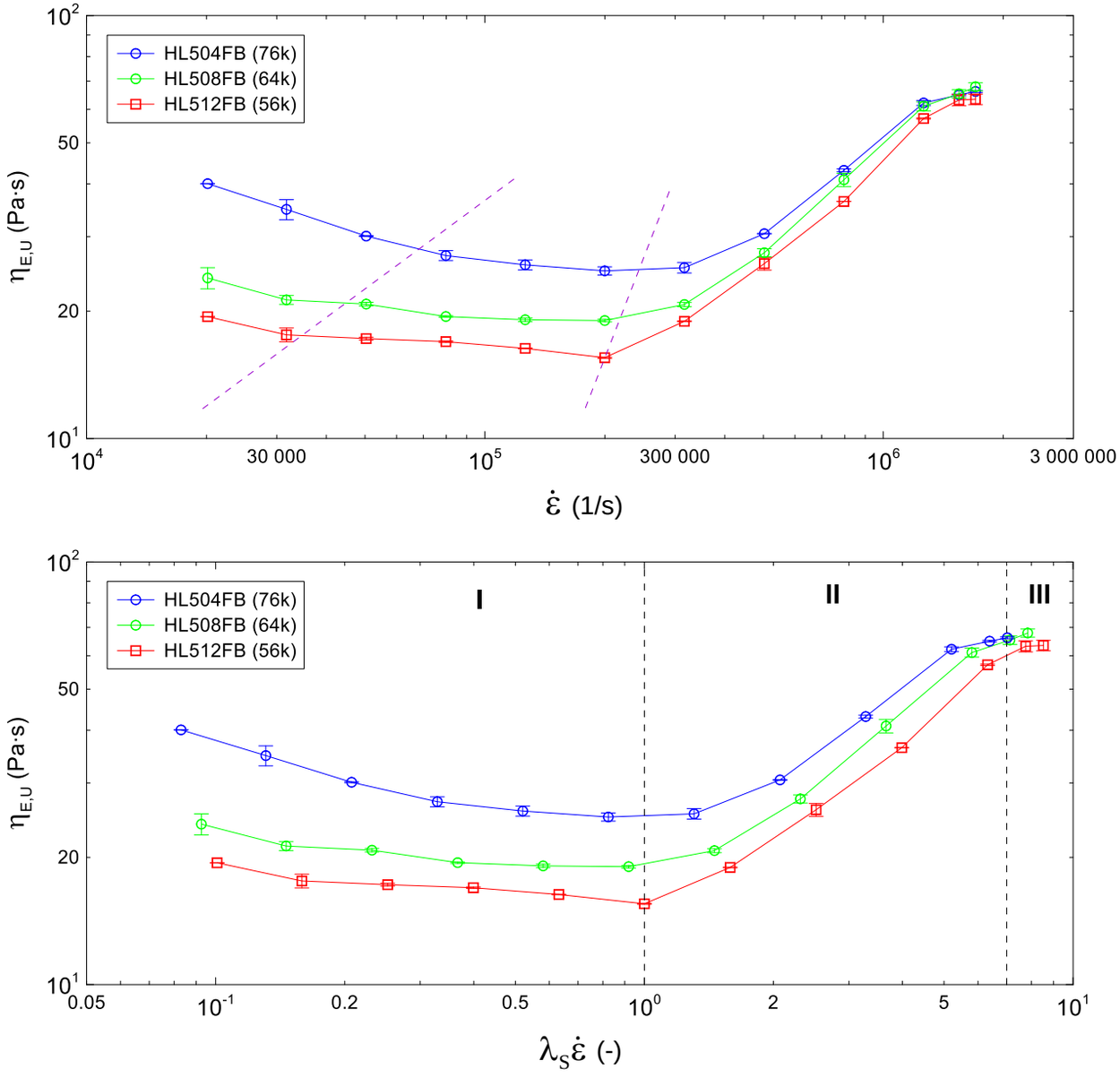

Figure 5 Uniaxial extensional viscosity, $\eta_{E,U}$, plotted as a function of the extensional strain rate (top) and chain stretch Weissenberg number (bottom) at 230 °C for three linear isotactic polypropylenes differing in weight-average molecular weight.

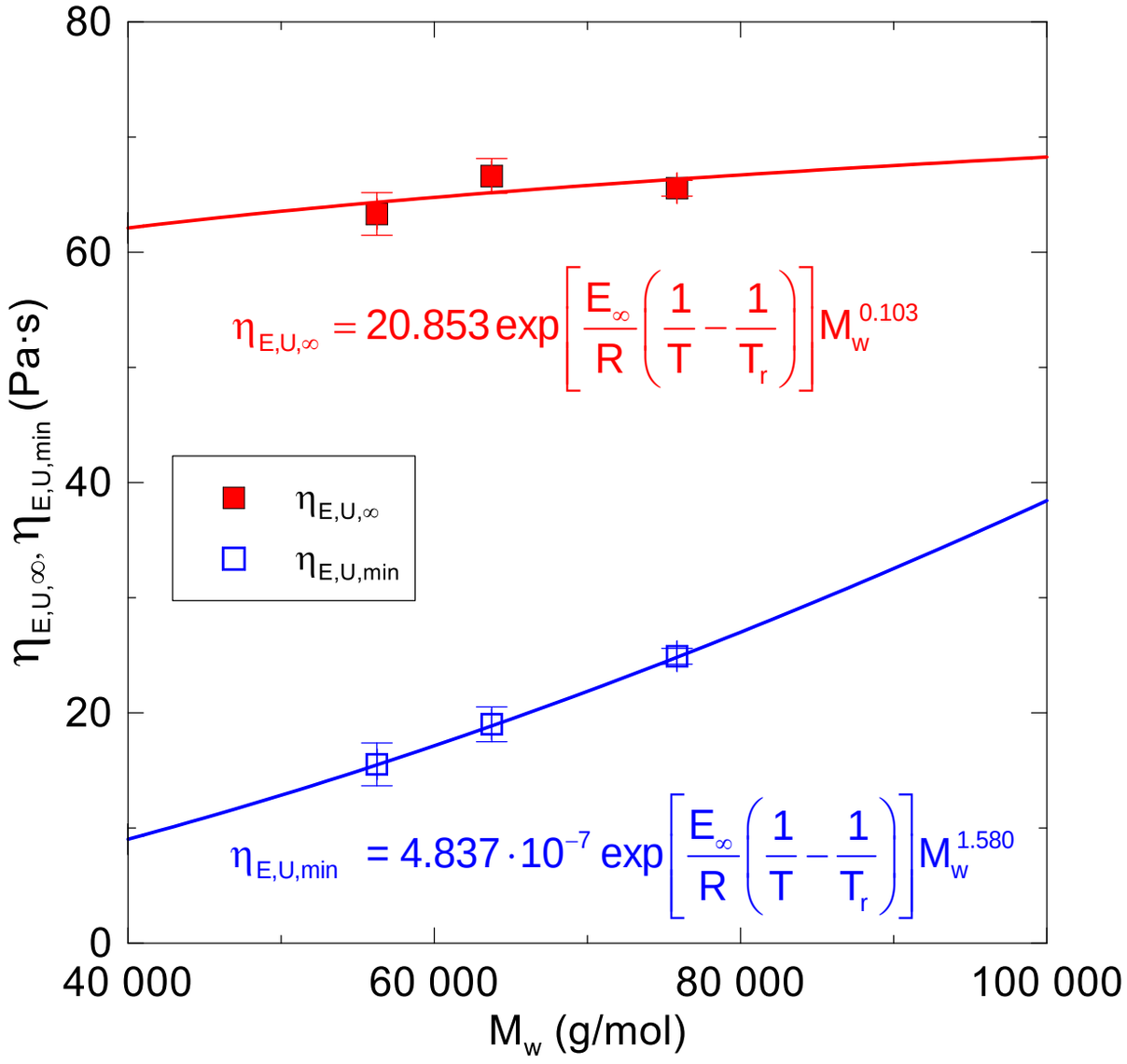

Figure 6 The plateau value of uniaxial extensional viscosity at the highest extensional strain rates, $\eta_{E,\infty}$, and the minimum uniaxial extensional viscosity, $\eta_{E,U,min}$, plotted as a function of weigh-average molecular weight, M_w, for linear isotactic polypropylene at 230 °C. In this case, T and T_r are equal to 503.15 K (i.e. 230 °C).

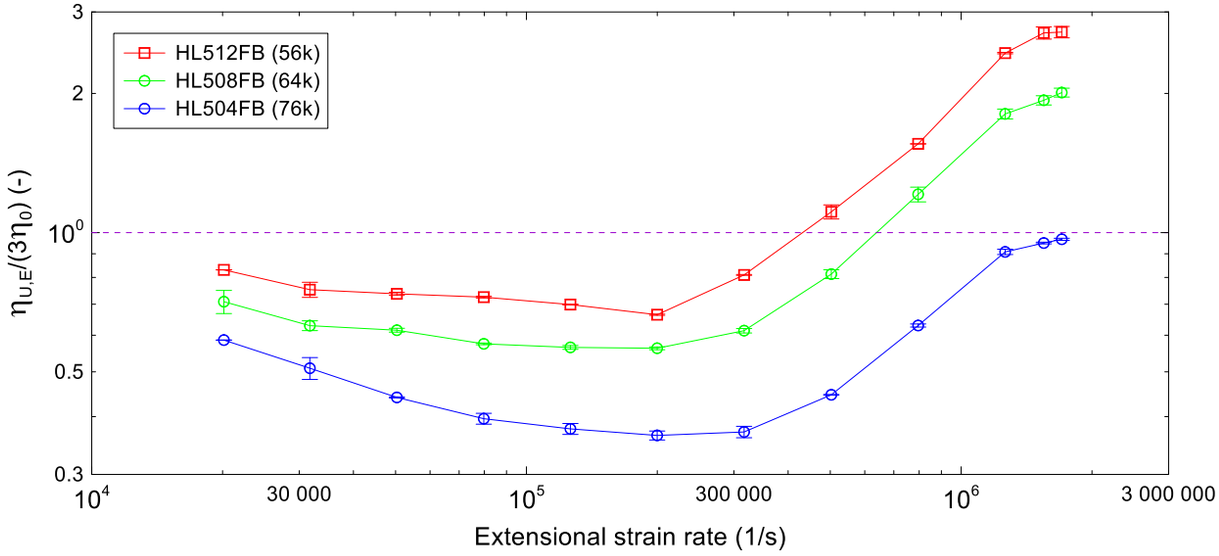

Figure 7 Uniaxial extensional viscosity, $\eta_{E,U}$, normalized by the three times zero-shear rate viscosity, η_0, plotted as a function of the extensional strain rate at 230 °C for three linear isotactic polypropylenes differing in weight-average molecular weight.

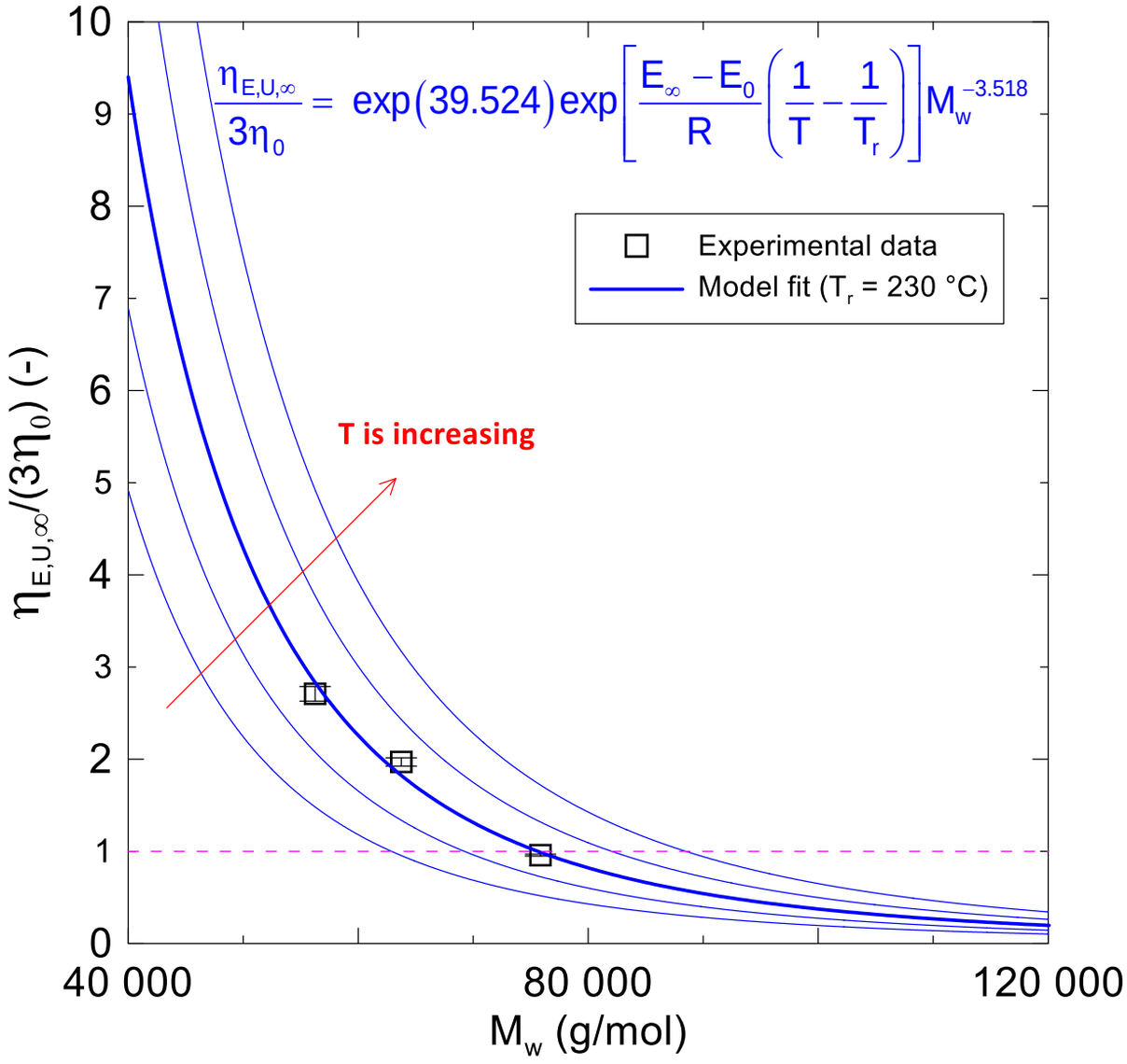

Figure 8 The plateau value of uniaxial extensional viscosity at the highest extensional strain rates, $\eta_{E,U,\infty}$, normalized by the three times zero-shear rate viscosity, η_0, (i.e. the extensional strain hardening at the maximum chain stretch) plotted as a function of weigh-average molecular weight, M_w, for linear isotactic polypropylene at 230 °C. The lines represent predictions of Eq.12 for different temperatures by using the flow activation energies given in Table 1.

HL504FB

Area 1

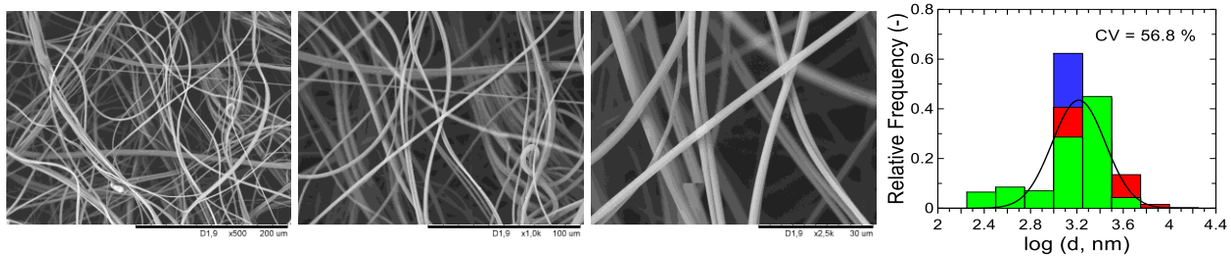

Area 2

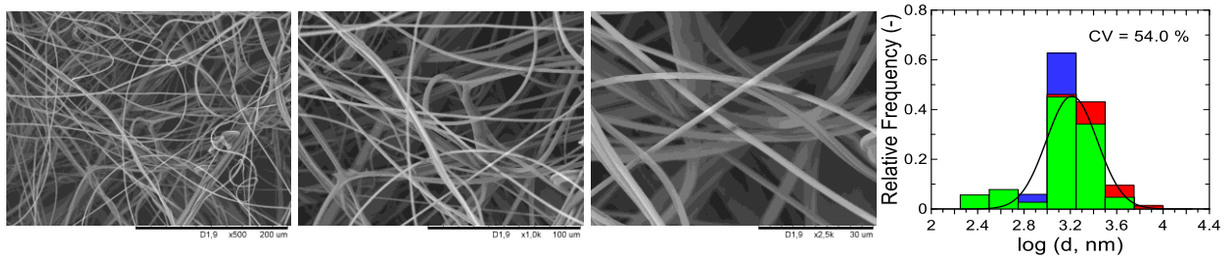

Figure 9 SEM images for L-PP sample (HL504FB), T = 250 °C, belt speed 5 m/min and DCD = 500 mm at two different areas and different magnifications (left – 500×, middle – 1000×, right – 2500×) together with corresponding final overall fiber diameter distribution.

Area 1

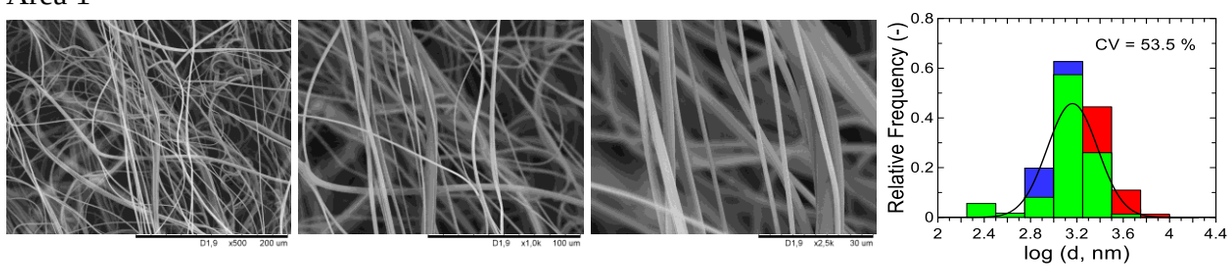

Area 2

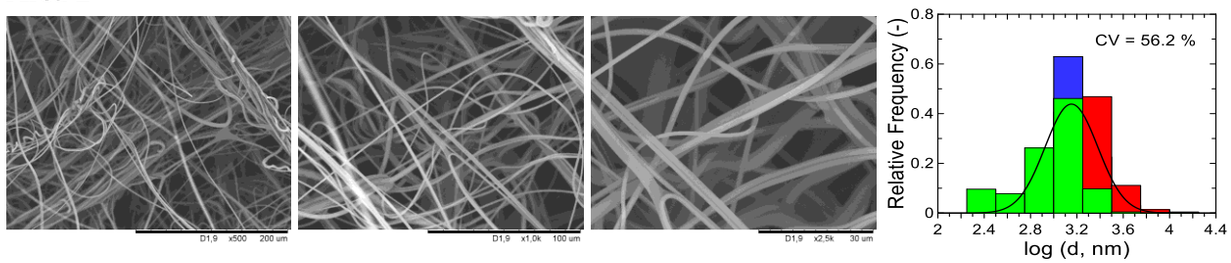

Figure 10 SEM images for L-PP sample (HL504FB), T = 270 °C, belt speed 5 m/min and DCD = 500 mm at two different areas and different magnifications (left – 500×, middle – 1000×, right – 2500×) together with corresponding final overall fiber diameter distribution.

HL508FB

Area 1

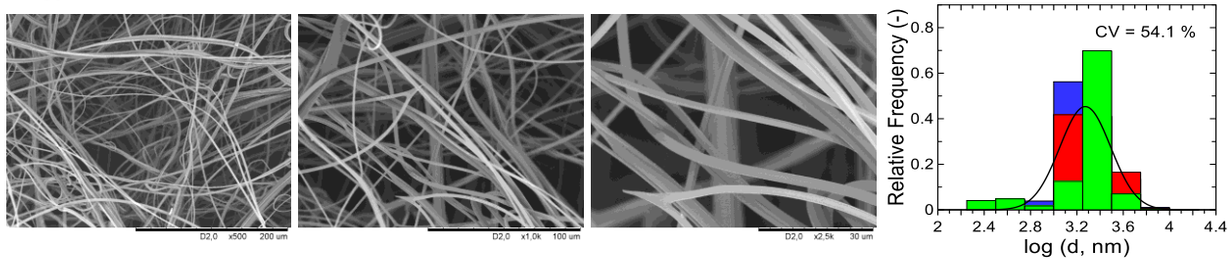

Area 2

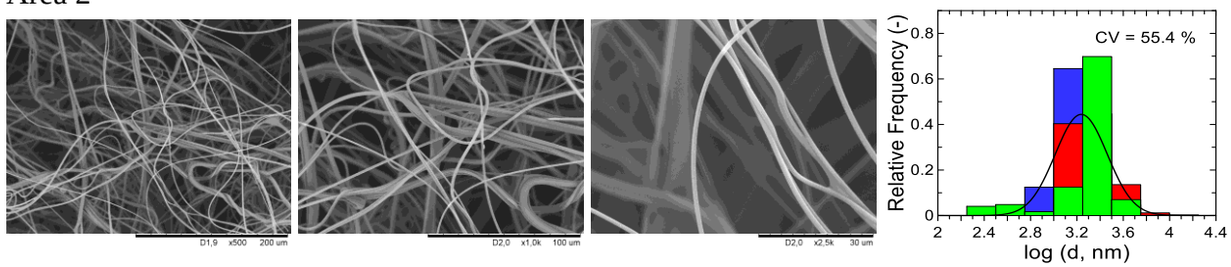

Figure 11 SEM images for L-PP sample (HL508FB), T = 250 °C, belt speed 5 m/min and DCD = 500 mm at two different areas and different magnifications (left – 500×, middle – 1000×, right – 2500×) together with corresponding final overall fiber diameter distribution.

Area 1

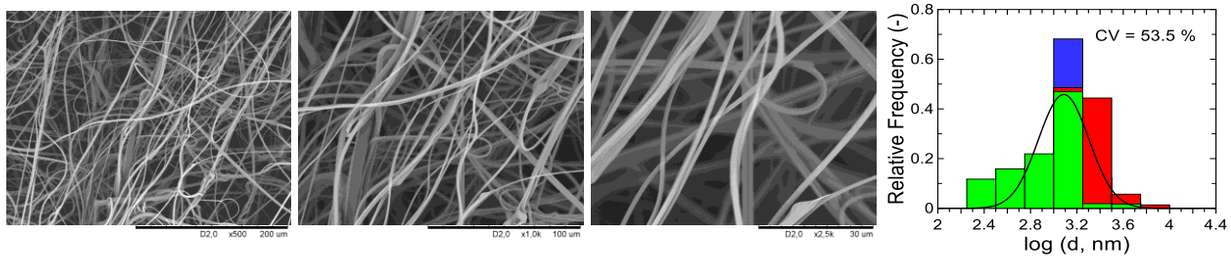

Area 2

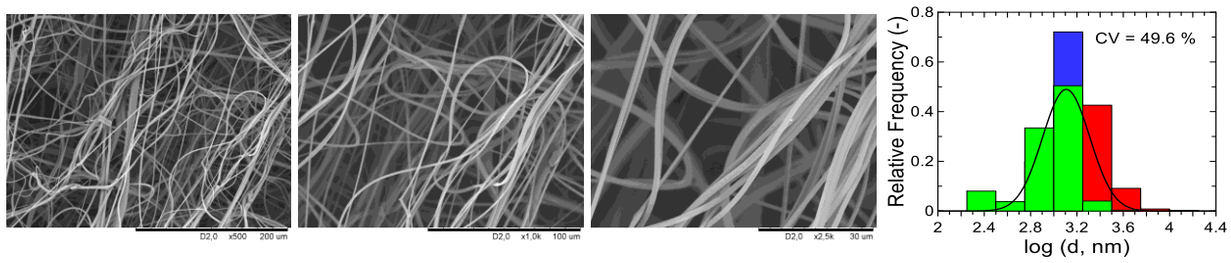

Figure 12 SEM images for L-PP sample (HL508FB), T = 270 °C, belt speed 5 m/min and DCD = 500 mm at two different areas and different magnifications (left – 500×, middle – 1000×, right – 2500×) together with corresponding final overall fiber diameter distribution.

HL512FB

Area 1

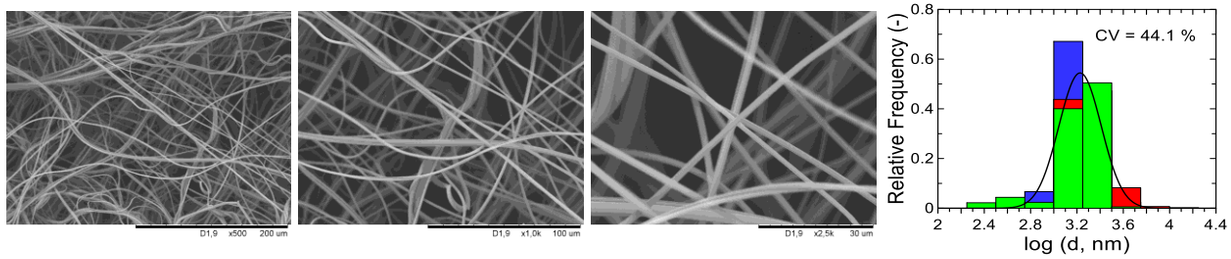

Area 2

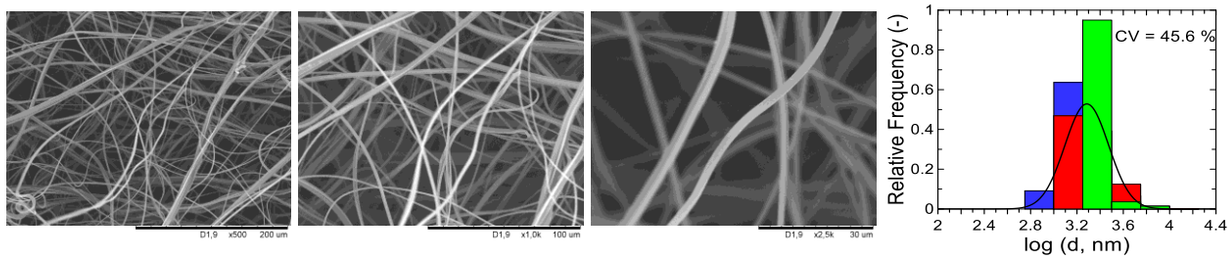

Figure 13 SEM images for L-PP sample (HL512FB), T = 250 °C, belt speed 5 m/min and DCD = 500 mm at two different areas and different magnifications (left – 500×, middle – 1000×, right – 2500×) together with corresponding final overall fiber diameter distribution.

Area 1

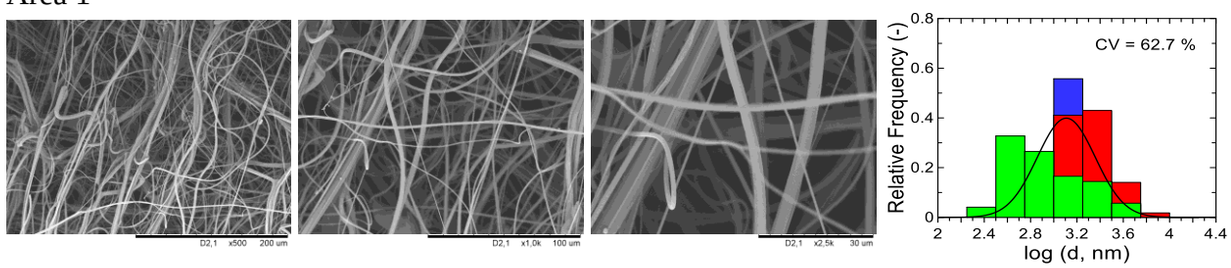

Area 2

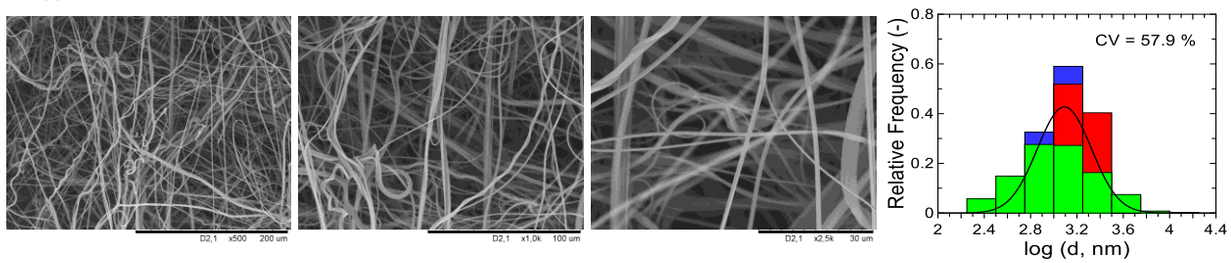

Figure 14 SEM images for L-PP sample (HL512FB), T = 270 °C, belt speed 5 m/min and DCD = 500 mm at two different areas and different magnifications (left – 500×, middle – 1000×, right – 2500×) together with corresponding final overall fiber diameter distribution.

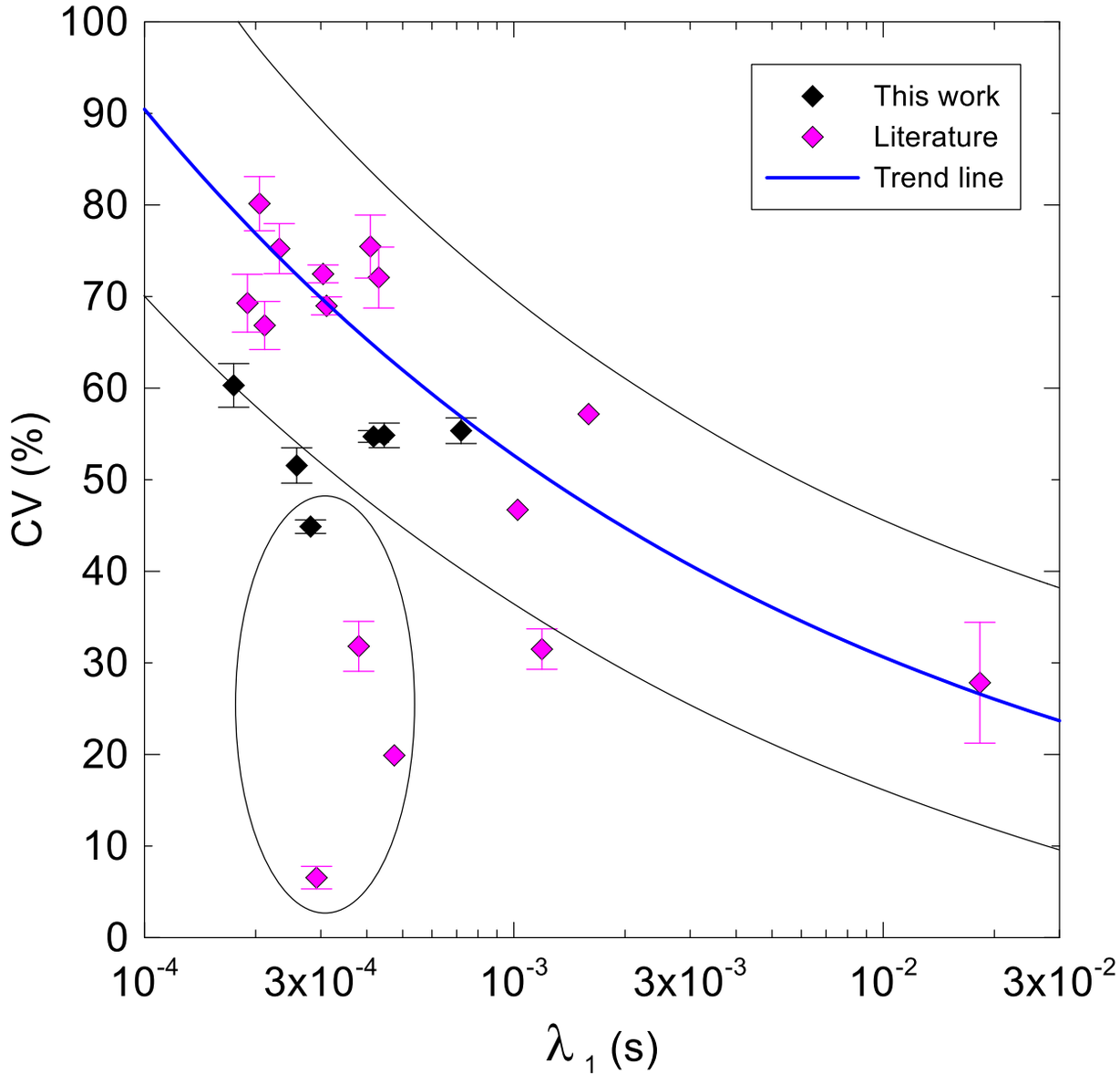

Figure 15 Coefficient of fiber diameter variation, *CV*, plotted as a function of the reptation-mode relaxation time, λ_1.

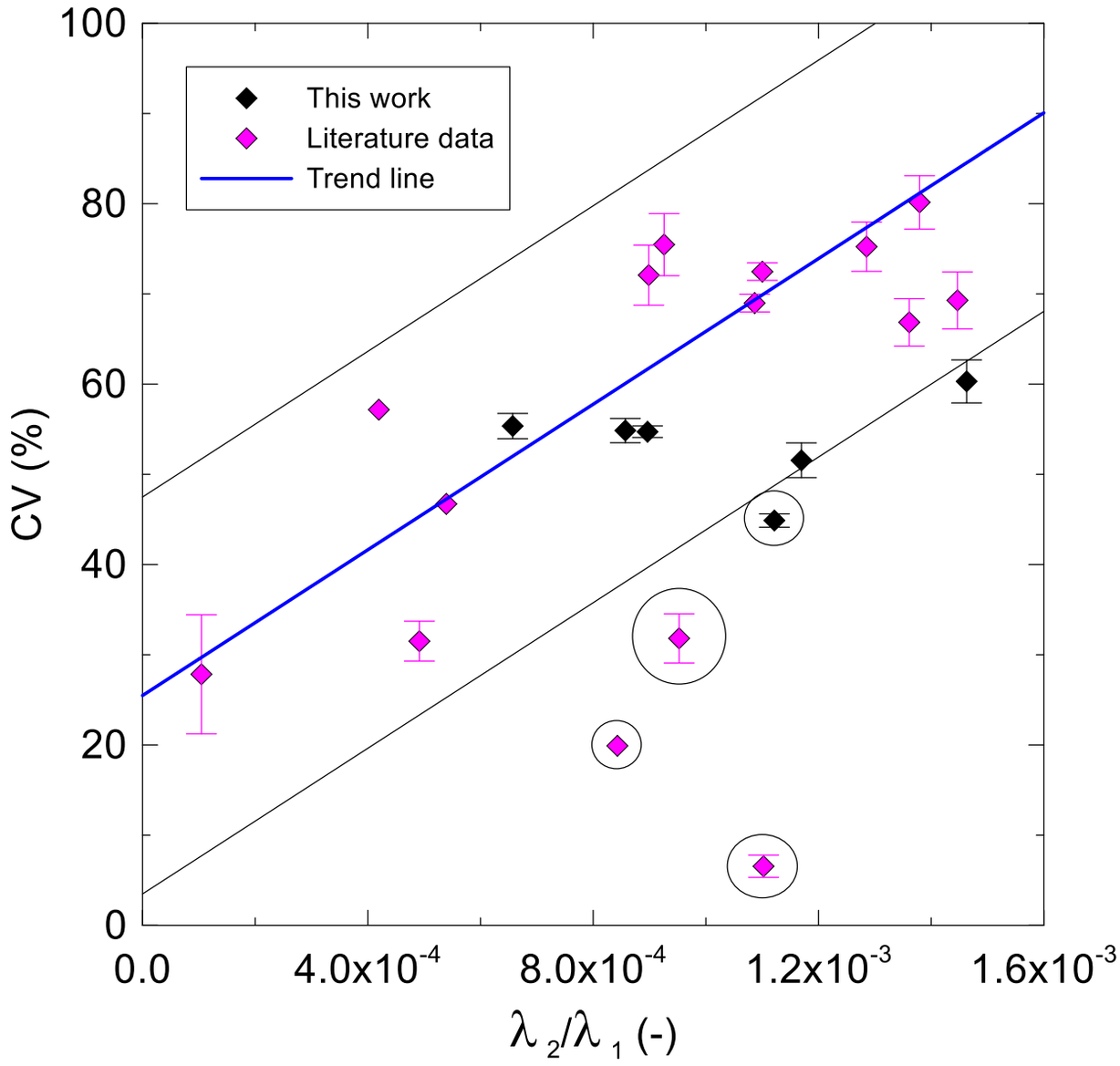

Figure 16 Coefficient of fiber diameter variation, *CV*, versus the ratio of the Rouse-mode reorientation time, λ_2, and the reptation-mode relaxation time, λ_1.

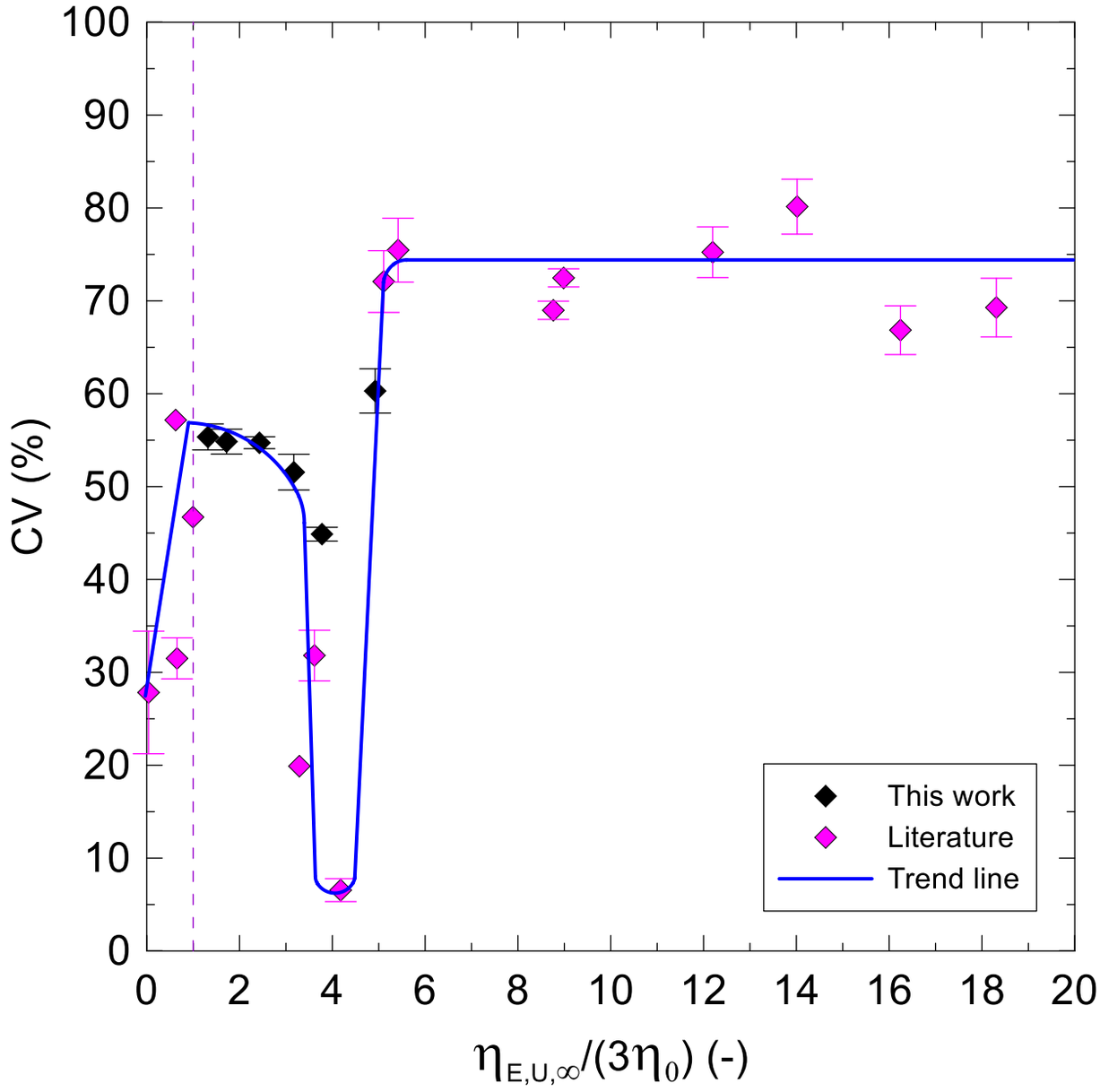

Figure 17 Coefficient of fiber diameter variation, *CV*, versus the maximum strain hardening in uniaxial extension, $\eta_{E,U,\infty}/(3\eta_0)$.

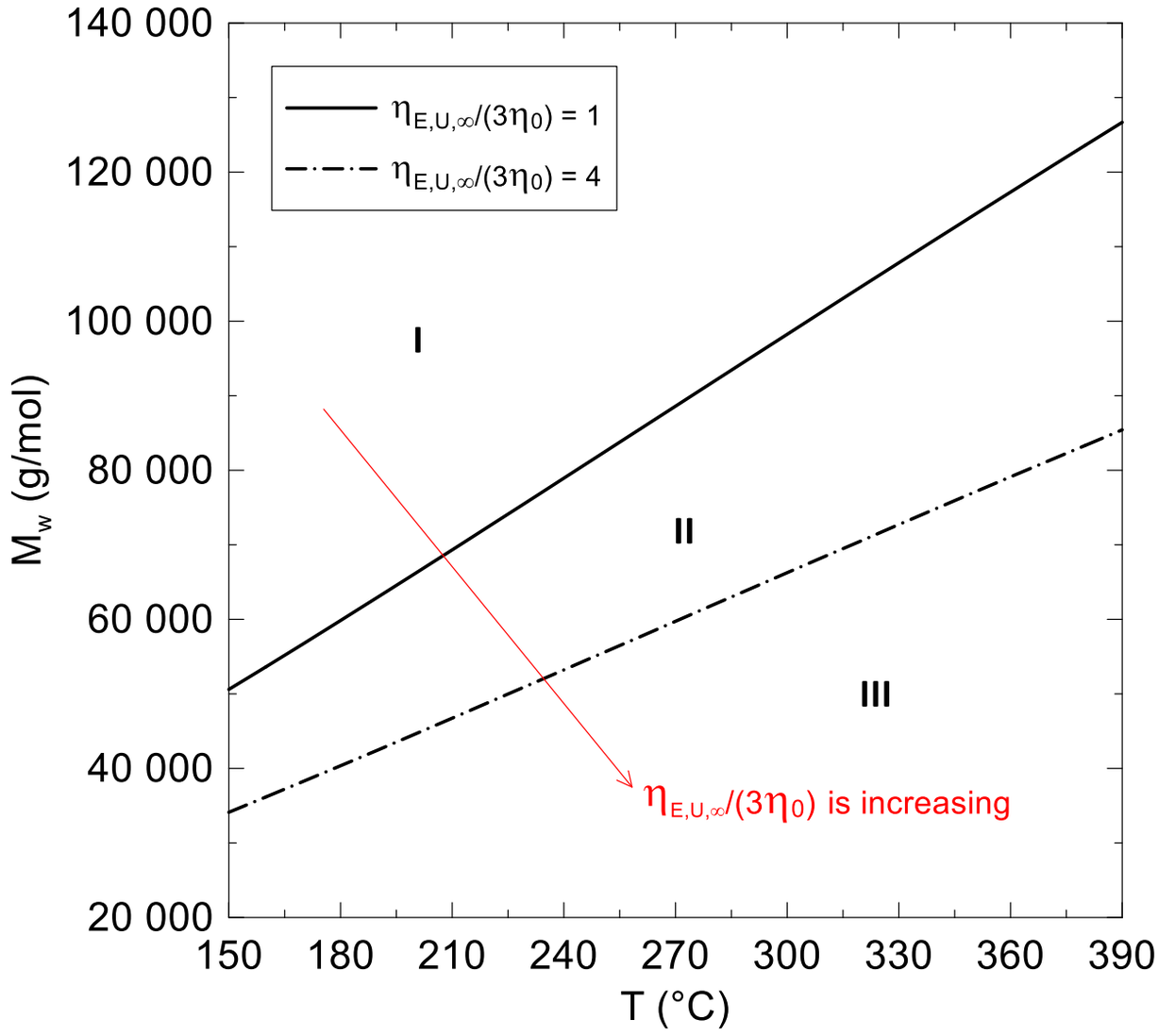

Figure 18 Influence of temperature on critical weight-average molecular weight, M_w, to achieve the given maximum strain hardenings in uniaxial extension, $\eta_{E,U,\infty}/(3\eta_0)$, according to Eq. 13 and the flow activation energies provided in Table 1.

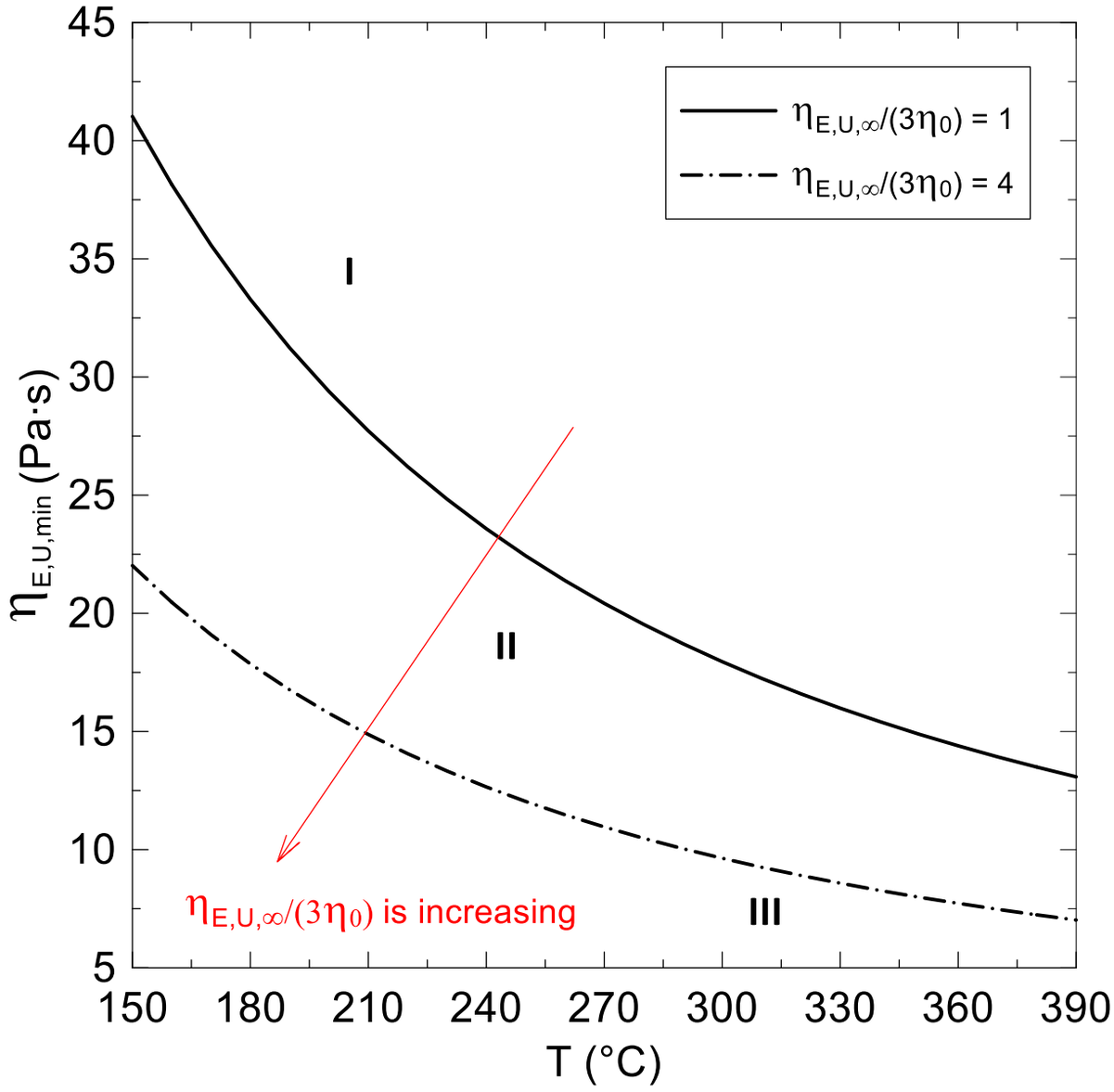

Figure 19 Influence of temperature on critical minimum uniaxial extensional viscosity, $\eta_{E,U,min}$, to reach the given maximum strain hardenings in uniaxial extension, $\eta_{E,U,\infty}/(3\eta_0)$ according to Eq.14 and the flow activation energies provided in Table 1.